Research Square

Preprints are preliminary reports that have not undergone peer review.
They should not be considered conclusive, used to inform clinical practice,
or referenced by the media as validated information.

# $Sm^{3+}$-Modified $ZnWO_4/YVO_4$ Heterostructure for Enhanced Photocatalytic Degradation of Crystal Violet and Sulfamethoxazole

**Lal Lianmawii**

lianmoyizd13@gmail.com

Mizoram University

**Research Article**

**Keywords:** $Sm^{3+}$-modified $ZnWO_4/YVO_4$ heterostructure, Photocatalytic degradation, Crystal Violet, Sulfamethoxazole, Wastewater remediation.

**Posted Date:** November 11th, 2026

**DOI:** https://doi.org/10.21203/rs.3.rs-11265132/v1

**License:** This work is licensed under a Creative Commons Attribution 4.0 International License.
Read Full License

**Additional Declarations:** No competing interests reported.

# $Sm^{3+}$-Modified $ZnWO_4/YVO_4$ Heterostructure for Enhanced Photocatalytic Degradation of Crystal Violet and Sulfamethoxazole

**Lal Lianmawii**

**Department of Chemistry, Mizoram University, Tanhril, Aizawl, Mizoram, India, 796004**

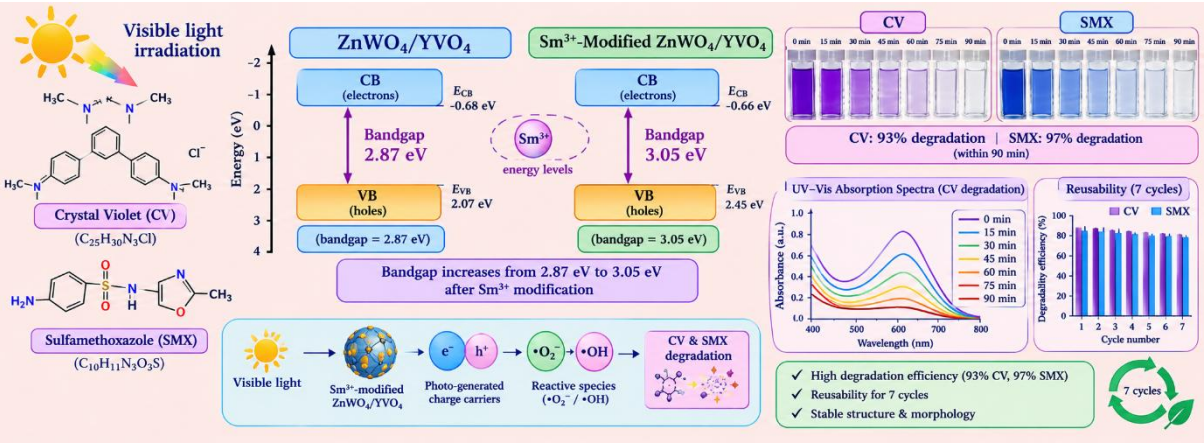
**Corresponding author: lianmoyizd13@gmail.com**

## Abstract

$Sm^{3+}$-modified $ZnWO_4/YVO_4$ ternary heterostructure was developed as a reusable photocatalyst for photocatalytic treatment of chemically diverse aquatic contaminants, Crystal Violet (CV) and sulfamethoxazole (SMX). The novelty lies in integrating a $ZnWO_4/YVO_4$ heterointerface with $Sm^{3+}$ modification, thereby combining interfacial charge separation with dopant-induced electronic/defect regulation, while demonstrating applicability to both dye and pharmaceutical pollutants. XRD, Raman, XPS, SEM, TEM/HRTEM, SAED and AFM confirmed the coexistence and crystalline integrity of monoclinic $ZnWO_4$ and tetragonal $YVO_4$, successful Sm incorporation, and transformation toward finer, elongated nanostructures. The crystallite size was reduced to approximately 20 nm upon $Sm^{3+}$ modification, as estimated from the XRD data using the Debye–Scherrer equation. UV–Vis analysis showed a reduction in effective optical band gap from 3.05 to 2.87 eV with a red-shifted absorption edge from 406 to 432 nm. TRPL lifetime increased from 3.12 to 5.78 ms, while EIS revealed a marked reduction in charge-transfer resistance to 260 Ω, supporting improved carrier separation and migration. Under irradiation, $Sm^{3+}/ZnWO_4/YVO_4$ achieved 93% CV and 97% SMX degradation within 90 min, compared with 78% and 58%, respectively, for unmodified $ZnWO_4/YVO_4$. The processes followed pseudo-first-order kinetics with $R^2$ values of 0.992 for CV and 0.981 for SMX. Optimal conditions were 20 mg/L catalyst dosage, pH 3 for CV and pH 5 for SMX. The catalyst retained 87% CV and 89% SMX removal after seven cycles. Enhanced activity is attributed to $Sm^{3+}$-assisted charge transfer, reduced recombination, and ROS generation, highlighting potential for reusable wastewater remediation. The findings establish a structure property performance relationship for efficient contaminant removal and practical real-world application.

**Keywords**

$Sm^{3+}$-modified $ZnWO_4/YVO_4$ heterostructure, Photocatalytic degradation, Crystal Violet, Sulfamethoxazole, Wastewater remediation.




## 1. Introduction

The rapid growth of pharmaceutical, textile, dyeing, and chemical industries has resulted in the continuous discharge of persistent organic contaminants into aquatic environments[1]. Among these pollutants, synthetic dyes and pharmaceutical residues are of particular concern because of their chemical stability, high water solubility, biological activity, and resistance to conventional wastewater-treatment processes[2]. Crystal Violet (CV) is a cationic triphenylmethane dye extensively used in textile, printing, biological staining, and related industrial applications[3]. Its release into water is undesirable because of its persistence and reported toxicological effects. CV possesses an extended conjugated aromatic structure and a strong visible-light absorption band, which makes its removal from contaminated water particularly important[4]. Photocatalytic oxidation has consequently received considerable attention as an advanced treatment process because photogenerated charge carriers can generate highly reactive species capable of attacking the conjugated chromophore and progressively converting the dye into smaller molecular products[5]. Previous investigations have demonstrated that CV degradation can involve hydroxyl radicals, superoxide species, singlet oxygen, and photogenerated holes, with the relative contribution depending strongly on the photocatalyst and reaction conditions[6]. In parallel with dye pollution, the occurrence of sulfamethoxazole (SMX), a widely used sulfonamide antibiotic, has become an important environmental concern. SMX is frequently detected in wastewater and aquatic environments because conventional biological and physicochemical treatment processes do not always achieve complete removal[7]. Its continuous introduction into water systems is particularly problematic because residual antibiotics and their transformation products may contribute to

the development and dissemination of antimicrobial resistance[8]. Recent reviews have identified SMX as one of the frequently encountered pharmaceutical contaminants and have highlighted heterogeneous photocatalysis as a promising approach for its removal because semiconductor-generated reactive oxygen species can attack chemically stable functional groups within the SMX molecule[9]. Importantly, removal of the parent SMX molecule does not necessarily imply complete detoxification or mineralization, since several transformation products can remain in the treated solution[10]. Consequently, the development of photocatalysts capable of both rapid pollutant removal and extensive oxidative transformation is still necessary. Photocatalytic degradation is fundamentally governed by the generation, separation, migration, and interfacial utilization of photogenerated electrons and holes[11]. Upon irradiation with photons having energy equal to or greater than the semiconductor band gap, electrons are promoted from the valence band (VB) to the conduction band (CB), leaving positively charged holes in the VB. Efficient photocatalysis therefore requires suppression of electron–hole recombination and effective transfer of the charge carriers to surface reaction sites[12]. The photogenerated holes can oxidize adsorbed water or hydroxyl groups to produce •OH, while conduction-band electrons can reduce dissolved oxygen to generate $\bullet O_2^-$, followed by other reactive oxygen species depending on the redox potentials and solution conditions[13]. These highly reactive species can attack aromatic rings, heteroatoms, conjugated bonds, and other susceptible functional groups in organic pollutants. For CV, reported transformation routes include N-demethylation, hydroxylation, cleavage of the conjugated triphenylmethane structure, removal of aromatic groups, and subsequent ring-opening reactions[14]. For SMX, reported photocatalytic pathways include hydroxylation, isomerization, S–N bond cleavage, fragmentation, and opening of the isoxazole ring. The development of heterostructure and doped semiconductor photocatalysts provides an effective strategy for addressing the limitations of individual photocatalysts[15]. Combining two semiconductors with suitable electronic structures can promote interfacial charge separation, extend the optical response, increase the number of surface-active sites, and facilitate directional migration of photogenerated charge carriers[16]. Tungstate-based semiconductors are particularly attractive because the W–O framework can participate in photoinduced redox processes, while their electronic structure can be modified through compositional engineering and heterojunction formation. $ZnWO_4$ is a structurally stable metal tungstate with a monoclinic wolframite-type structure and has been investigated as a photocatalytic semiconductor[17]. Nevertheless, like many single-component photocatalysts, its practical photocatalytic efficiency can be restricted by rapid recombination of photogenerated charge carriers and limited utilization of the solar spectrum[18]. The formation

of semiconductor heterostructures has therefore been explored to improve charge separation and photocatalytic activity; for example, $ZnWO_4$-based heterostructures have been demonstrated to modify light absorption and improve photocatalytic performance compared with the individual component[19]. $YVO_4$ provides an attractive complementary oxide component for constructing a $ZnWO_4$-based heterostructure. $YVO_4$ possesses a tetragonal zircon-type structure containing $VO_4^{3-}$ tetrahedral units and exhibits characteristic electronic and optical properties arising from the V–O framework[20]. Coupling $YVO_4$ with $ZnWO_4$ can provide an interfacial pathway for photogenerated charge transfer and may facilitate spatial separation of electrons and holes[21]. The intimate contact between the two semiconductor phases can consequently reduce bulk charge recombination and increase the probability that charge carriers participate in surface redox reactions. Incorporation of a rare-earth dopant such as $Sm^{3+}$ provides an additional route for tuning the electronic and defect structure of the composite. $Sm^{3+}$ incorporation can modify the local lattice environment, introduce charge-compensation defects, and influence charge-carrier trapping and migration[22]. Studies of $Sm^{3+}$-modified tungsten-oxide systems demonstrate that rare-earth incorporation can alter the structural and optical characteristics of the host lattice, providing a basis for using $Sm^{3+}$ as a structural/electronic modifier rather than simply as an additional component[23]. The incorporation of $Sm^{3+}$ into $ZnWO_4/YVO_4$ is therefore expected to provide a synergistic combination of heterojunction formation and dopant-induced electronic modification[24]. A possible photocatalytic process can be described as follows: under irradiation, $ZnWO_4$ and $YVO_4$ absorb photons and generate electron–hole pairs; interfacial charge migration between the two semiconductor phases promotes charge separation, while $Sm^{3+}$-associated defect states may act as charge-trapping or transfer sites. The resulting electrons can interact with dissolved $O_2$ to produce superoxide-related species, whereas photogenerated holes can oxidize surface $H_2O/OH^-$ to produce hydroxyl radicals.

Accordingly, the present study investigates the synthesis, structural, morphological, optical, and photocatalytic properties of $Sm^{3+}/ZnWO_4/YVO_4$ and evaluates its performance toward the degradation of Crystal Violet (CV) and sulfamethoxazole (SMX) under light irradiation. The novelty of this work lies in the development of a $Sm^{3+}$-modified $ZnWO_4/YVO_4$ ternary heterostructure that combines the advantages of heterojunction formation with rare-earth-ion modification to improve light utilization, charge separation, and photocatalytic efficiency. The integration of $ZnWO_4$ and $YVO_4$ is expected to facilitate interfacial charge transfer and suppress the recombination of photogenerated electron–hole pairs, while $Sm^{3+}$ incorporation

can modify the local electronic structure and defect environment of the composite. The use of two chemically distinct pollutants, namely the cationic triphenylmethane dye CV and the sulfonamide antibiotic SMX, further demonstrates the potential versatility of the developed photocatalyst toward different classes of emerging contaminants. The study further evaluates the photocatalytic kinetics, influence of operational parameters, reactive species involved in the degradation process, and catalyst reusability to establish the structure–property–performance relationship of the $Sm^{3+}/ZnWO_4/YVO_4$ heterostructure. To the best of our knowledge, limited studies have systematically investigated $Sm^{3+}$-modified $ZnWO_4/YVO_4$ for the simultaneous photocatalytic treatment of dye and pharmaceutical contaminants.

## 2. Materials and Methods

### Materials

Zinc nitrate hexahydrate ($Zn(NO_3)_2{\cdot}6H_2O$), sodium tungstate dihydrate ($Na_2WO_4{\cdot}2H_2O$), yttrium nitrate hexahydrate ($Y(NO_3)_3{\cdot}6H_2O$), ammonium metavanadate ($NH_4VO_3$), and samarium nitrate hexahydrate ($Sm(NO_3)_3{\cdot}6H_2O$) were employed as the precursor materials for the synthesis of the $Sm^{3+}$-modified $ZnWO_4/YVO_4$ ternary heterostructure. Crystal Violet (CV; $C_{25}H_{30}ClN_3$) and sulfamethoxazole (SMX; $C_{10}H_{11}N_3O_3S$) were selected as representative model pollutants for evaluating the photocatalytic degradation performance of the synthesized materials.

### Hydrothermal Synthesis of $Sm^{3+}$-Modified $ZnWO_4/YVO_4$

$Sm^{3+}$-modified $ZnWO_4/YVO_4$ ternary heterostructure was synthesized through a hydrothermal route using zinc nitrate hexahydrate ($Zn(NO_3)_2{\cdot}6H_2O$), sodium tungstate dihydrate ($Na_2WO_4{\cdot}2H_2O$), yttrium nitrate hexahydrate ($Y(NO_3)_3{\cdot}6H_2O$), ammonium metavanadate ($NH_4VO_3$), and samarium nitrate hexahydrate ($Sm(NO_3)_3{\cdot}6H_2O$) as the respective Zn, W, Y, V, and Sm precursors. $Zn(NO_3)_2{\cdot}6H_2O$ and $Na_2WO_4{\cdot}2H_2O$ were separately dissolved in deionized water to maintain a 1:1 molar ratio of $Zn^{2+}$:$WO_4^{2-}$. Similarly, $Y(NO_3)_3{\cdot}6H_2O$ and $NH_4VO_3$ were separately dissolved to obtain a 1:1 molar ratio of $Y^{3+}$:$VO_4^{3-}$. The precursor solutions were stirred individually until homogeneous and subsequently mixed under continuous magnetic stirring. $Sm(NO_3)_3{\cdot}6H_2O$ was then added to the mixed $ZnWO_4/YVO_4$ precursor suspension to introduce the desired $Sm^{3+}$ modification. The resulting mixture was continuously stirred to ensure homogeneous distribution of the constituent ions. The obtained precursor suspension was transferred into a Teflon-lined stainless-steel autoclave at 200 °C for the selected reaction duration. After completion of the hydrothermal reaction, the autoclave

was allowed to cool naturally to room temperature. The resulting precipitate was separated by centrifugation at 8000 rpm, followed by repeated washing with deionized water and ethanol to remove residual soluble species and impurities. The washed product was subsequently dried at the selected temperature to obtain the $Sm^{3+}$-modified $ZnWO_4/YVO_4$ ternary heterostructure.

## 3. Characterization

The crystal structure of the prepared heterostructure was investigated using an X-ray diffractometer (XRD, Rigaku MiniFlex 600, Japan) with Cu Kα radiation (λ = 1.5406 Å). The surface morphology of the heterostructure was examined using a field-emission scanning electron microscope (FESEM, JEOL JSM-7610F, Japan). The nanostructure, lattice fringes, and interfacial characteristics were further investigated using a transmission electron microscope (TEM, JEOL JEM-2100, Japan) and a high-resolution transmission electron microscope (HRTEM, FEI Tecnai G2 F20, USA), equipped with selected-area electron diffraction (SAED). The elemental composition and spatial distribution of the constituent elements were analyzed using an energy-dispersive X-ray spectroscopy (EDX/EDS) detector coupled with the TEM/SEM system (Oxford Instruments X-Max, UK), along with elemental mapping analysis. The surface chemical composition, oxidation states, and chemical bonding characteristics of the heterostructure were investigated using X-ray photoelectron spectroscopy (XPS, Thermo Scientific K-Alpha, USA). The structural bonding and vibrational properties were analyzed using a Raman spectrometer (HORIBA LabRAM HR Evolution). The surface roughness and topographical features were characterized using an atomic force microscope (AFM, Bruker Dimension Icon, USA). The specific surface area, pore volume, and pore-size distribution of the heterostructure were determined using a Brunauer–Emmett–Teller (BET) surface-area analyzer (Micromeritics ASAP 2020, USA). The optical absorption characteristics and band-gap energy of the heterostructure were evaluated using a UV–Visible diffuse reflectance spectrophotometer (UV–Vis DRS, Shimadzu UV-2600, Japan). A UV–Visible spectrophotometer (Shimadzu UV-1800, Japan) was employed to monitor the photocatalytic degradation of the dye. The mineralization efficiency of the degraded dye solution was further evaluated by measuring the total organic carbon (TOC) using a TOC analyzer (Shimadzu TOC-L, Japan).

## 4. Results and discussions

### 4.1 X-ray diffraction analysis

The crystalline structures and phase composition of the synthesized $ZnWO_4/YVO_4$ heterostructure and Sm-modified $ZnWO_4/YVO_4$ were investigated by powder X-ray diffraction (XRD), and the corresponding patterns are presented in Fig. 1 (a,b). The diffraction profiles demonstrate the coexistence of crystalline $ZnWO_4$ and $YVO_4$ phases, indicating the successful formation of the heterostructured material. For the $ZnWO_4/YVO_4$ heterostructure Fig. 1(a), the diffraction reflections originating from $ZnWO_4$ can be indexed to the monoclinic wolframite-type structure of $ZnWO_4$, which is consistent with JCPDS No. 15-0774. Literature reports assign the characteristic $ZnWO_4$ reflections at approximately 15.3°, 18.7°, 23.7°, 24.3°, 30.4°, 31.1°, 36.2°, 40.9°, 44.2°, 45.8°, 49.9° and 51.5° to the corresponding $ZnWO_4$ crystallographic planes[25]. In particular, the reflection near 30.4° arises from closely spaced (111) and (−111) planes, while the reflection around 36.2° can contain contributions from the (021)/(002) planes. Similarly, the reflection near 41° may contain contributions from the (121)/(−121) planes. These closely spaced reflections are characteristic of monoclinic $ZnWO_4$. The $YVO_4$ component exhibits the characteristic diffraction pattern of tetragonal zircon-type $YVO_4$, in agreement with JCPDS No. 17-0341. Reported $YVO_4$ patterns show characteristic reflections including (200), (112), (312), and (400), with the (200) reflection occurring at approximately 25° and the (112) reflection near 33–34°. The preservation of these reflections in the composite confirms the presence of crystalline $YVO_4$[26]. The simultaneous observation of reflections attributable to both monoclinic $ZnWO_4$ and tetragonal $YVO_4$, without the appearance of obvious additional impurity reflections, provides evidence for the formation of the $ZnWO_4/YVO_4$ heterostructure.

For the Sm-modified $ZnWO_4/YVO_4$ sample Fig. 1(b), the principal diffraction reflections of both $ZnWO_4$ and $YVO_4$ are retained. This indicates that Sm modification does not destroy the fundamental crystal structures of the $ZnWO_4$ and $YVO_4$ components. The absence of additional crystalline Sm-containing reflections suggests that no detectable crystalline Sm-containing secondary phase was formed under the present conditions. Compared with the unmodified $ZnWO_4/YVO_4$ sample, the Sm-modified material may exhibit slight peak broadening and a decrease in relative diffraction intensity. Such changes can be associated with reduced crystallite size, lattice distortion, defect formation, and microstrain generated during Sm incorporation or surface modification. Similar changes in diffraction peak width and intensity have been reported for modified $ZnWO_4$ systems, where changes in crystallinity and lattice strain affect the XRD profile. The average crystallite size of the synthesized photocatalysts was estimated using the Debye–Scherrer equation 1:

$$D = \frac{k\lambda}{\beta cos\theta} \quad (1)$$

where D is the average crystallite size, k is the Scherrer constant (0.9), $\boldsymbol{\lambda}$ is the wavelength of the incident Cu Kα radiation (0.15406 nm), β is the full width at half maximum (FWHM) of the selected diffraction peak in radians, and $\boldsymbol{\theta}$ is the corresponding Bragg angle. The calculated average crystallite size was approximately 28 nm for $ZnWO_4/YVO_4$, whereas the crystallite size decreased to approximately 20 nm for Sm-modified $ZnWO_4/YVO_4$. The reduction in crystallite size following Sm modification may be attributed to the influence of Sm ions on the nucleation and crystal-growth processes. The incorporation or surface modification by Sm can inhibit the growth and aggregation of $ZnWO_4/YVO_4$ crystallites, resulting in smaller crystalline domains. The reduced crystallite size may also be accompanied by increased lattice disorder and microstrain, as reflected by the broadening of the XRD reflections. The decrease in crystallite size from 28 to 20 nm is potentially beneficial for photocatalytic activity because smaller crystallites provide a larger fraction of surface atoms and can increase the accessible surface area and shorten the migration distance of photogenerated charge carriers.

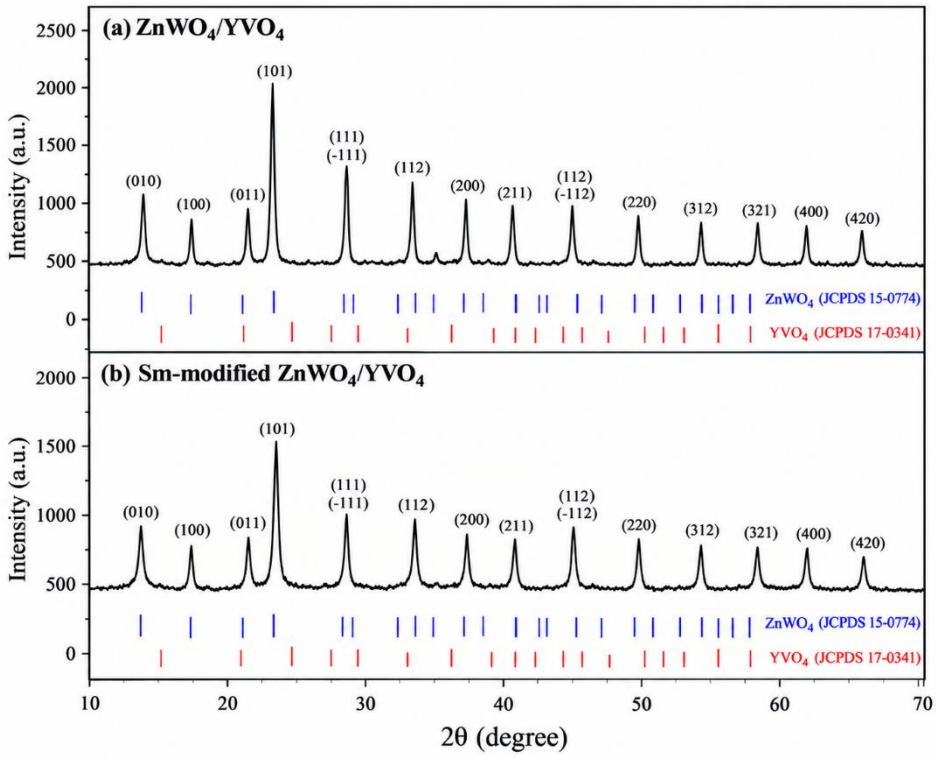



Figure 1. XRD patterns of (a) $ZnWO_4/YVO_4$ and (b) Sm-modified $ZnWO_4/YVO_4$ heterostructures. The diffraction reflections are indexed according to monoclinic $ZnWO_4$

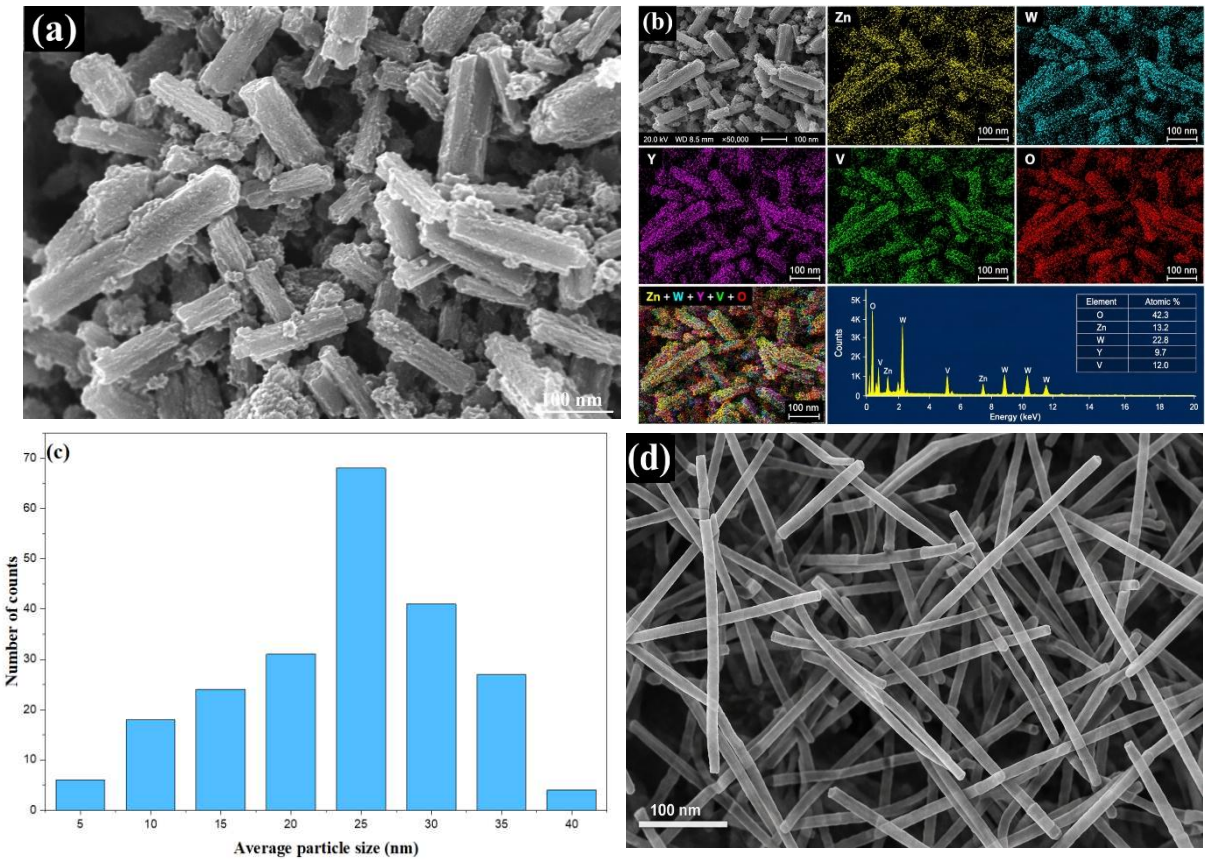
(JCPDS No. 15-0774) and tetragonal $YVO_4$ (JCPDS No. 17-0341). The vertical reference lines indicate the corresponding standard diffraction positions.

### 4.2 SEM Morphological and Elemental Analysis

The morphological and elemental characteristics of the as-prepared $ZnWO_4/YVO_4$ heterostructure and Sm-modified composite are presented in Fig. 2. The $ZnWO_4/YVO_4$ heterostructure Fig. 2(a) exhibits an elongated rod-like morphology with relatively compact aggregation of particles. The rods display a non-uniform size distribution and variations in morphology at the particle level. The corresponding EDX analysis and elemental mapping Fig. 2(b) confirm the presence of Zn, W, Y, V, and O, which are the constituent elements of the $ZnWO_4/YVO_4$ heterostructure[27]. The spatial distributions of Zn and W are associated with the $ZnWO_4$ phase, whereas Y and V correspond to the $YVO_4$ phase. The relatively homogeneous distribution of these elements throughout the analyzed region indicates the successful formation of the heterostructure. The average particle size calculated using ImageJ software was approximately 25 nm for the $ZnWO_4/YVO_4$ heterostructure Fig. 2(c).

In comparison, the morphology of the Sm-modified $ZnWO_4/YVO_4$ composite is considerably altered. As shown in Fig. 2(d), the Sm-modified sample exhibits highly elongated and thinner rod/wire-like structures. This morphological transformation suggests that the incorporation of $Sm^{3+}$ ions influence the nucleation and crystal-growth processes during composite formation. $Sm^{3+}$ ions may interact with hydroxyl groups and oxygen-containing species during synthesis and can modify the surface energies and relative growth rates of different crystallographic planes. The morphological transformation may be associated with $Sm^{3+}$-induced changes in nucleation and crystal-growth kinetics. In addition, the different ionic radius, charge density, and coordination characteristics of $Sm^{3+}$ compared with the constituent cations may contribute to the modification of the crystal-growth process. The EDX spectrum and elemental mapping of the Sm-modified $ZnWO_4/YVO_4$ composite Fig. 2(e) confirm the presence of Zn, W, Y, V, O, and Sm, demonstrating the incorporation of samarium into the composite. The Sm elemental map shows a relatively homogeneous distribution throughout the analyzed region, while Zn, W, Y, V, and O are also distributed across the rod-like particles. The corresponding overlay image further demonstrates the spatial coexistence of these elements within the composite, supporting the formation of the Sm-modified heterostructure[28]. The average particle size calculated from the SEM images using ImageJ software was approximately 20 nm for the Sm-modified $ZnWO_4/YVO_4$ composite, which is slightly smaller than that of the pristine

$ZnWO_4/YVO_4$ heterostructure Fig. 2(f). The decrease in average particle size following $Sm^{3+}$ incorporation may be associated with the influence of $Sm^{3+}$ ions on the nucleation and crystal-growth processes, which can suppress particle growth and promote the formation of finer structures. The incorporation of $Sm^{3+}$ may also influence the electronic structure and charge-transfer behavior of the composite by introducing additional defect or localized electronic states[29]. These states may act as electron-trapping sites, potentially suppressing electron–hole recombination and improving the availability of charge carriers for photocatalytic reactions. Therefore, the incorporation of $Sm^{3+}$ may influence both the morphological evolution and charge-transfer properties of the $ZnWO_4/YVO_4$ heterostructure, potentially contributing to its enhanced photocatalytic performance.



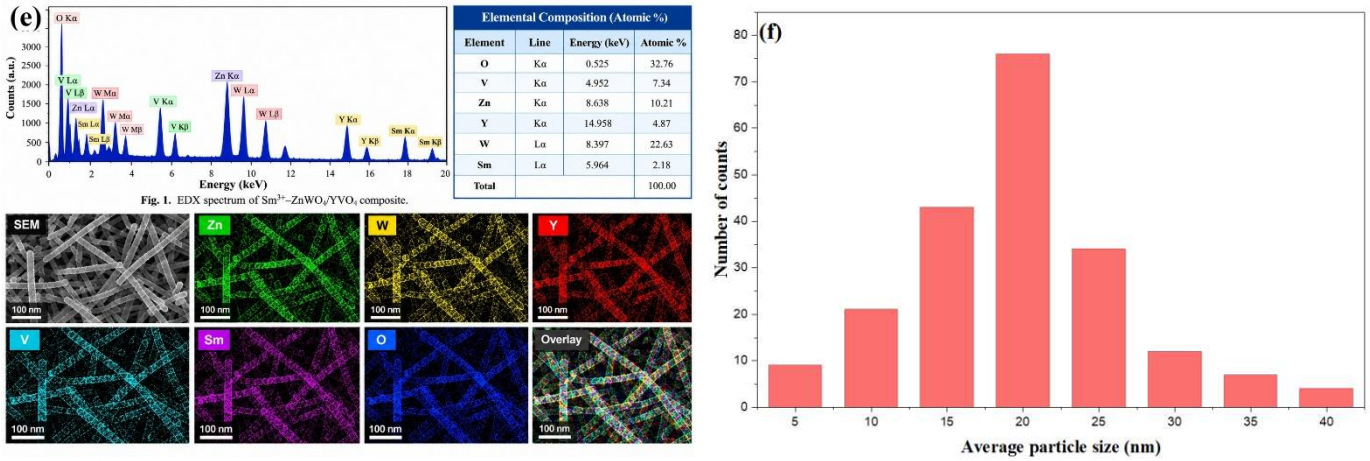



Fig. 1. EDX spectrum of $Sm^{3+}$–$ZnWO_4/YVO_4$ composite.

Figure 2. SEM morphological and elemental characterization of $ZnWO_4/YVO_4$ and Sm-modified $ZnWO_4/YVO_4$ composites: (a) SEM image of $ZnWO_4/YVO_4$, (b) EDX spectrum and elemental mapping, (c) ImageJ-based particle-size distribution, (d) SEM image of Sm-modified $ZnWO_4/YVO_4$, (e) EDX spectrum and elemental mapping of the Sm-modified composite (f) ImageJ-based particle-size distribution.

### 4.3 TEM Analysis

The transmission electron microscopy (TEM), high-resolution TEM (HRTEM), and selected-area electron diffraction (SAED) characteristics of the $ZnWO_4/YVO_4$ heterostructure and Sm-modified $ZnWO_4/YVO_4$ composite are presented in Fig. 3. For $ZnWO_4/YVO_4$ heterostructure, the low-magnification TEM image in Fig. 3(a) reveals the formation of well-defined elongated rod-like structures with relatively uniform contrast and some degree of aggregation. The observed anisotropic morphology is consistent with the rod-like morphology identified from the SEM analysis[30]. The coexistence of elongated structures and smaller attached particles suggests intimate contact between the constituent $ZnWO_4$ and $YVO_4$ phases, which is favorable for interfacial charge transfer in the heterostructure. The corresponding HRTEM image in Fig. 3(b) provides direct evidence of the crystalline nature of the $ZnWO_4/YVO_4$ heterostructure. Well-resolved and regularly spaced lattice fringes can be clearly observed within the rod-like structures, confirming the high degree of crystallinity of the synthesized material[31]. The measured interplanar spacings of approximately 0.221, 0.167, and 0.114 nm are associated with the selected crystalline planes indicated in the HRTEM image. The SAED pattern of $ZnWO_4/YVO_4$ in Fig. 3(c) exhibits a series of concentric diffraction rings composed of numerous bright diffraction spots. This ring-type diffraction pattern confirms the

polycrystalline nature of the material. The diffraction rings can be indexed to the (010), (101), (111), and (112) planes, consistent with the crystalline phases identified by XRD. The presence of multiple well-defined rings further confirms that the rod-like structures observed by TEM are composed of crystalline domains rather than amorphous material.

In contrast, the Sm-modified $ZnWO_4/YVO_4$ composite exhibits a noticeable morphological transformation, as shown in Fig. 3(d). The TEM image reveals the formation of highly elongated, thinner rod/wire-like structures with a more pronounced anisotropic morphology compared with the pristine $ZnWO_4/YVO_4$ sample. This observation agrees well with the SEM results and indicates that Sm modification influences the nucleation and subsequent crystal-growth process. The formation of thinner and more elongated structures may result from the interaction of $Sm^{3+}$ species with the growing $ZnWO_4/YVO_4$ crystallites, which can alter surface energies and preferential growth along specific crystallographic directions. The HRTEM image of the Sm-modified composite in Fig. 3(e) shows clear, continuous lattice fringes, demonstrating that the Sm modification preserves the crystalline nature of the $ZnWO_4/YVO_4$ framework. The enlarged inset provides additional evidence of the ordered lattice structure. The well-defined fringes indicate that the incorporation of Sm does not destroy the crystallinity of the heterostructure, in agreement with the XRD results. At the same time, slight lattice imperfections or local distortions may be introduced by Sm modification, which is consistent with the peak broadening and reduced crystallite size observed in the XRD analysis. The SAED pattern of the Sm-modified $ZnWO_4/YVO_4$ composite in Fig. 3(f) also displays distinct concentric diffraction rings with bright spots, confirming its polycrystalline crystalline structure[32]. The observed rings are indexed to the (010), (101), (111), and (112) planes. The persistence of these diffraction rings after Sm modification demonstrates that the fundamental crystalline structure of the $ZnWO_4/YVO_4$ heterostructure is maintained. Therefore, the TEM/HRTEM/SAED observations collectively confirm that Sm modification induces a morphological transformation toward thinner elongated structures while retaining the crystalline character of the $ZnWO_4/YVO_4$ heterostructure. The particle sizes estimated from the TEM images using ImageJ were approximately 29 nm for $ZnWO_4/YVO_4$ and 20 nm for Sm-modified $ZnWO_4/YVO_4$, which are closely consistent with the corresponding XRD crystallite sizes of 28 and 20 nm, respectively. The small difference observed for the pristine $ZnWO_4/YVO_4$ sample can be attributed to the distinction between particle size measured directly from TEM and crystallite size estimated from XRD. The close agreement between the two techniques confirms the nanoscale crystalline nature of the synthesized composites.

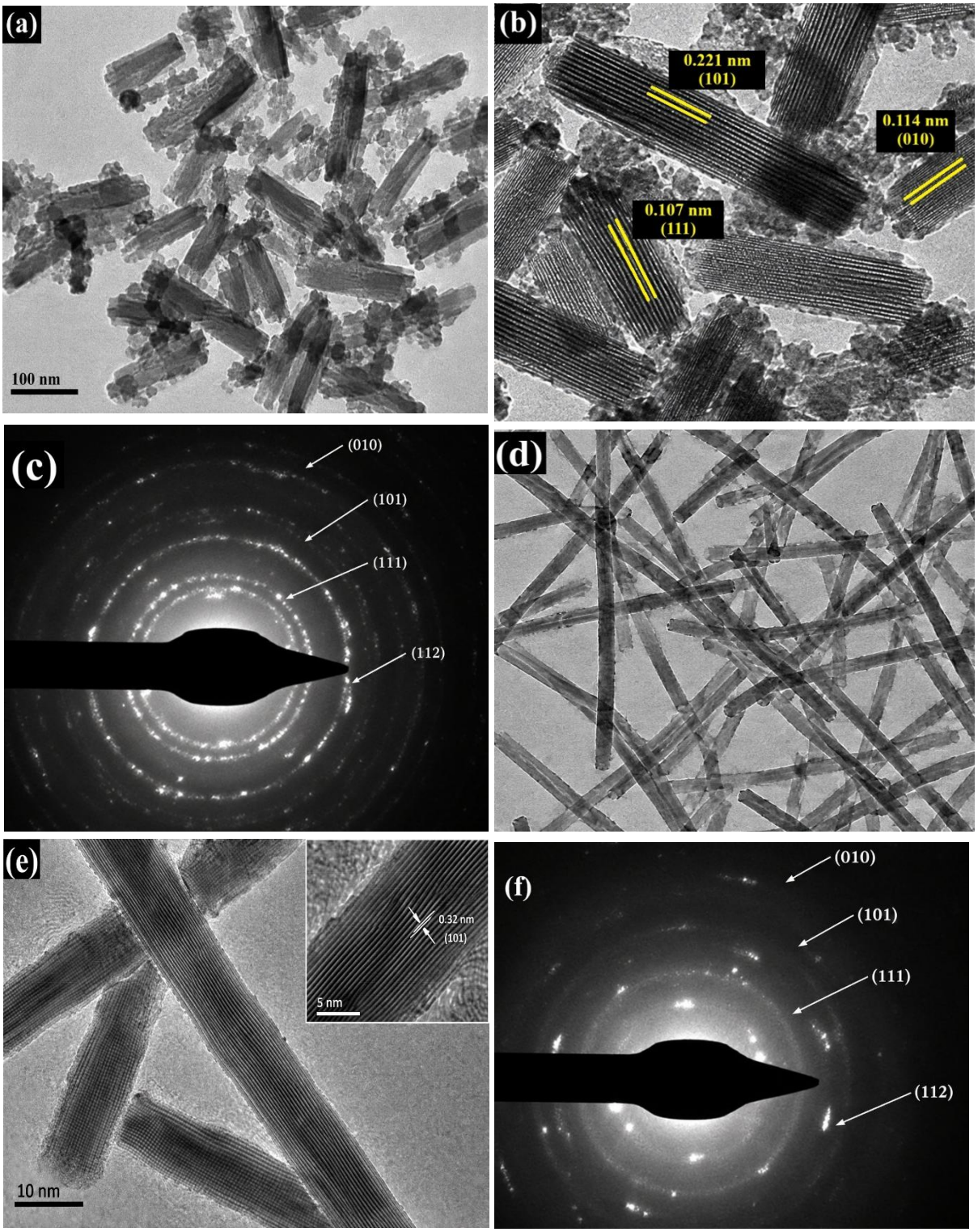



Figure 3. TEM and HRTEM analyses of the $ZnWO_4/YVO_4$ and Sm-modified $ZnWO_4/YVO_4$ composites: (a) low-magnification TEM image of $ZnWO_4/YVO_4$, (b) HRTEM image showing lattice fringes, (c) corresponding SAED pattern indexed to the selected crystallographic planes,

(d) low-magnification TEM image of Sm-modified $ZnWO_4/YVO_4$, (e) HRTEM image with enlarged lattice-fringe inset, and (f) corresponding SAED pattern of the Sm-modified composite.

### 4.4 AFM morphological analysis

The surface morphology and three-dimensional topographical characteristics of the prepared $ZnWO_4/YVO_4$ and Sm-modified $ZnWO_4/YVO_4$ samples were investigated by atomic force microscopy (AFM), as shown in Fig. 4(a,b). The corresponding 2D AFM height images and 3D surface-rendered images provide information about the particle distribution, surface texture, and height variation across a $2 \times 2\ \mu m^2$ scanned area. Fig. 4(a) represents the $ZnWO_4/YVO_4$ heterostructure. The AFM image reveals a relatively compact surface composed of elongated rod-like/irregularly elongated features with noticeable aggregation. The 3D topographical image confirms pronounced height variations across the surface, indicating that the rod-like particles are distributed at different vertical levels. The height scale extends to approximately 120 nm, demonstrating a relatively rough and heterogeneous surface morphology. This topographical feature is consistent with the rod-like morphology observed from SEM and TEM. Fig. 4(b) corresponds to the Sm-modified $ZnWO_4/YVO_4$ composite[33]. A more pronounced elongated wire/rod-like surface structure can be observed, with numerous thinner features distributed across the scanned region. Compared with the $ZnWO_4/YVO_4$ sample, the Sm-modified material exhibits a more interconnected and finely structured surface morphology. The corresponding 3D AFM image further demonstrates the distribution of these elongated structures over the substrate, with a maximum height of approximately 100 nm according to the displayed height scale[34]. The altered surface topography can be associated with the influence of $Sm^{3+}$ incorporation on nucleation and crystal-growth processes. Overall, the AFM observations support the SEM and TEM results, demonstrating that $Sm^{3+}$ modification induces a morphological transformation toward finer, more elongated structures. Such surface modification can increase the accessible surface area and expose additional active sites, which may be beneficial for photocatalytic reactions.

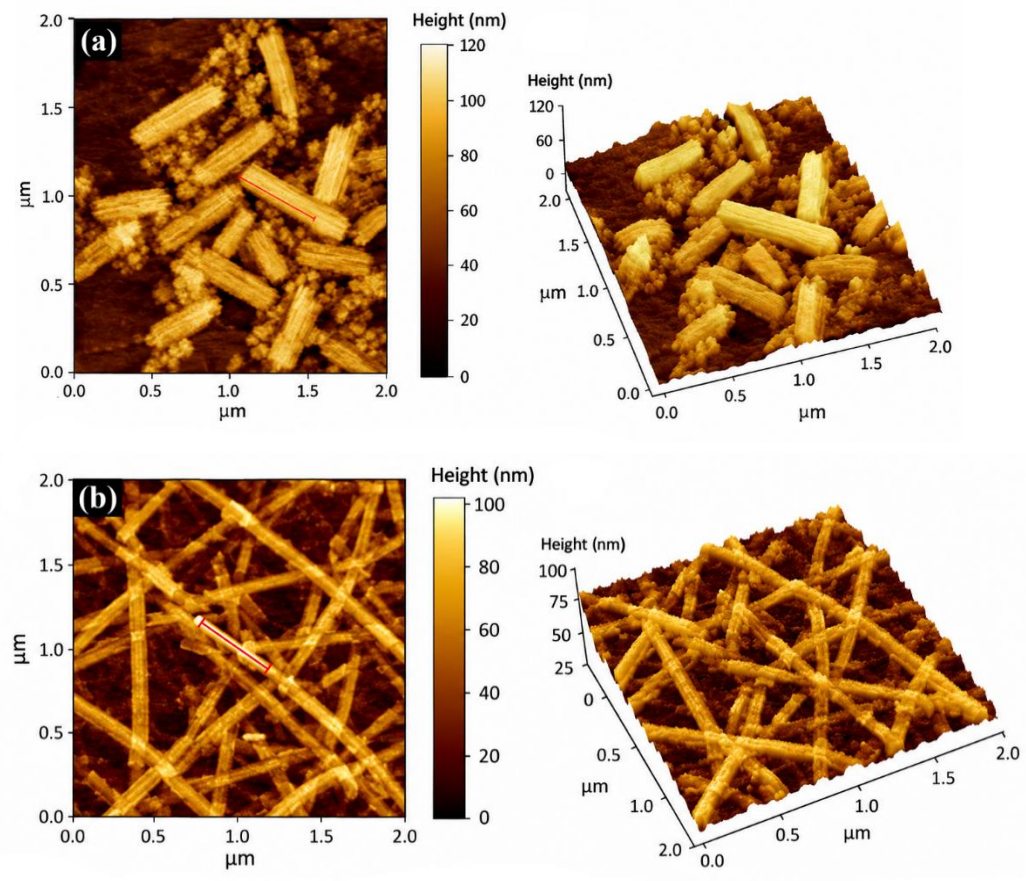



Figure 4. AFM surface morphology and three-dimensional topographical images of (a) $ZnWO_4/YVO_4$ and (b) Sm-modified $ZnWO_4/YVO_4$ heterostructures.

### 4.5 BET surface area and $N_2$ adsorption–desorption analysis

The $N_2$ adsorption–desorption isotherms of $ZnWO_4/YVO_4$ and Sm–$ZnWO_4/YVO_4$ are presented in Fig. 5. Both samples exhibit a characteristic Type III adsorption isotherm, accompanied by a distinct hysteresis between the adsorption and desorption branches, indicating the presence of textural porosity and capillary condensation within the aggregated structures. The adsorption amount increases progressively with increasing relative pressure ($P/P_0$), with a more pronounced increase in the higher-pressure region, suggesting weak adsorbate–adsorbent interactions and the contribution of interparticle voids. The $ZnWO_4/YVO_4$ sample exhibited a specific surface area of approximately 34 $m^2\ g^{-1}$, whereas the $Sm^{3+}$-modified $ZnWO_4/YVO_4$ exhibited a specific surface area of approximately 26 $m^2\ g^{-1}$. The decrease in particle size after Sm modification can provide a larger number of exposed surface sites and interparticle voids, which is favorable for adsorption of pollutant molecules and photocatalytic

reactions[35]. The comparatively higher $N_2$ uptake of the Sm-modified sample further suggests an increase in accessible surface area/textural porosity. Thus, Sm modification effectively alters the surface texture of $ZnWO_4/YVO_4$ and can contribute to its enhanced photocatalytic performance.

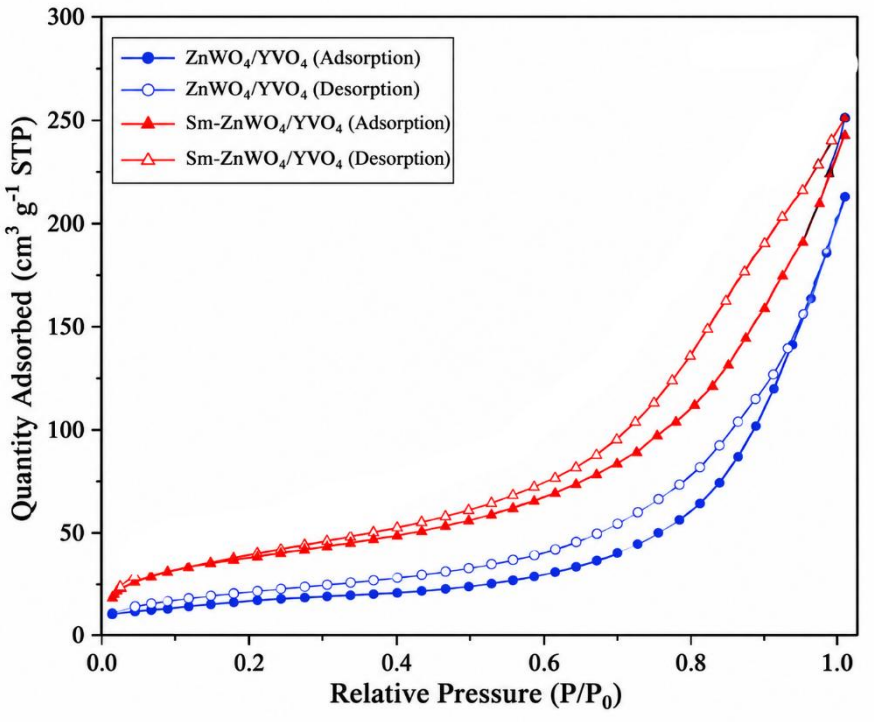



Figure 5. $N_2$ adsorption–desorption isotherms of $ZnWO_4/YVO_4$ and Sm–$ZnWO_4/YVO_4$ exhibiting Type III isotherm characteristics.

### 4.6 FTIR analysis of $ZnWO_4/YVO_4$ and Sm-modified $ZnWO_4/YVO_4$

The FTIR spectra of $ZnWO_4/YVO_4$ and $Sm^{3+}$-modified $ZnWO_4/YVO_4$ can be interpreted based on the characteristic vibrational modes of the tungstate, vanadate, hydroxyl, and adsorbed-water groups given in Fig 6. The broad absorption band appearing around 3200–3500 $cm^{-1}$ can be assigned to the stretching vibration of surface O–H groups, mainly associated with adsorbed moisture. The band near ~1600–1650 $cm^{-1}$ corresponds to the bending vibration of molecular H–O–H from surface-adsorbed water[27]. These bands are commonly observed in metal-oxide photocatalysts. In the lower-wavenumber region, the bands between approximately 400 and 900 $cm^{-1}$ are characteristic of the metal–oxygen framework. For $ZnWO_4$, vibrations in this region are associated with W–O stretching/bending, Zn–O vibrations and Zn–O–W linkages,

while the $WO_6/ZnO_6$ octahedral units contribute strongly to the fingerprint region[36]. $ZnWO_4$ spectra show characteristic features around ~470–600, ~700–830 and ~870 $cm^{-1}$.

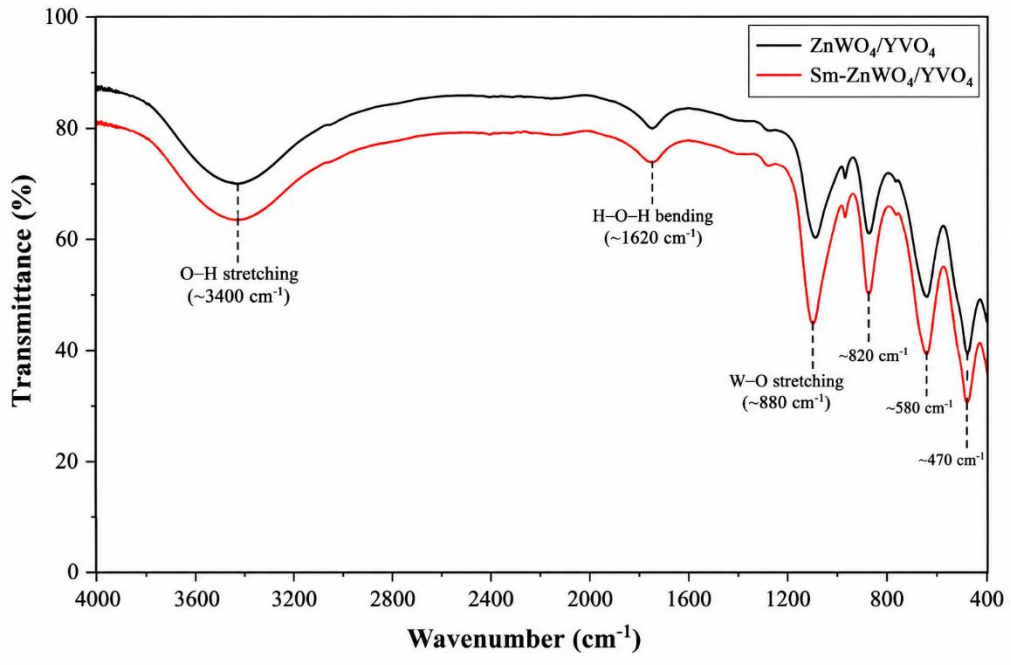



Figure 6. FTIR spectra of $ZnWO_4/YVO_4$ and Sm-modified $ZnWO_4/YVO_4$ showing characteristic O–H, H–O–H and metal–oxygen vibrational modes.

## 4.7 XPS analysis

X-ray photoelectron spectroscopy (XPS) was employed to investigate the elemental composition and chemical states of the $Sm^{3+}$-modified $ZnWO_4/YVO_4$ heterostructure Figure 7. The survey spectrum confirms the presence of Zn, W, Y, V, O and Sm, together with a weak C 1s signal originating mainly from adventitious surface carbon. The high-resolution Zn 2p spectrum displays two characteristic peaks at approximately 1021.7 and 1044.6 eV, corresponding to Zn $2p_{3/2}$ and Zn $2p_{1/2}$, respectively, confirming the presence of $Zn^{2+}$ in the $ZnWO_4$ component. The W 4f spectrum exhibits two prominent contributions at approximately 34.2 and 36.4 eV, assigned to W $4f_{7/2}$ and W $4f_{5/2}$, respectively, characteristic of $W^{6+}$ [37]. The V 2p spectrum shows peaks at approximately 516.1 and 523.6 eV, corresponding to V $2p_{3/2}$ and V $2p_{1/2}$, indicating the presence of $V^{5+}$ in $YVO_4$. The Y 3d region presents the characteristic spin–orbit doublet at approximately 156.8 and 158.7 eV, assigned to Y $3d_{5/2}$ and Y $3d_{3/2}$, respectively, consistent with $Y^{3+}$[38]. Importantly, the Sm 3d spectrum confirms the incorporation of Sm species into the heterostructure, with the characteristic Sm 3d doublet and associated

satellite features. The O 1s spectrum can be deconvoluted into three components, attributed to lattice oxygen ($O^{2-}$), oxygen associated with surface defects/oxygen vacancies, and surface-adsorbed oxygen or hydroxyl species[39]. The presence of these surface oxygen species may provide additional active sites for adsorption and reactive oxygen species generation during photocatalysis. The C 1s spectrum consists mainly of the C–C/C=C component at approximately 284.8 eV, together with higher-binding-energy contributions associated with C–O and O–C=O species. Overall, the XPS results confirm the successful coexistence of Zn, W, Y, V, O and Sm in the $Sm^{3+}$-modified $ZnWO_4/YVO_4$ heterostructure and support the formation of the chemically integrated heterostructure. The presence of Sm species and surface oxygen-defect-related components may contribute to enhanced interfacial charge transfer and improved photocatalytic activity toward SMX degradation.

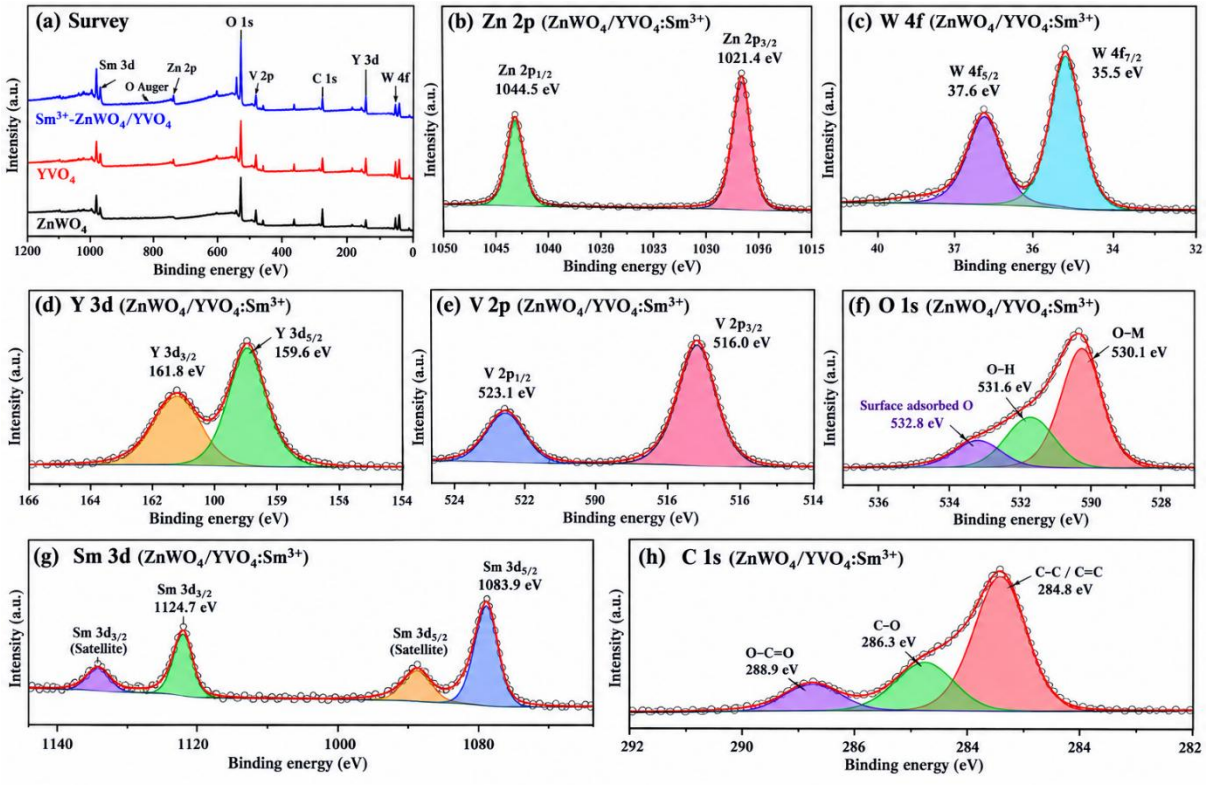



Figure 7. XPS survey and high-resolution deconvoluted spectra of the $Sm^{3+}$-modified $ZnWO_4/YVO_4$ heterostructure: (a) survey spectrum, (b) Zn 2p, (c) W 4f, (d) V 2p, (e) Y 3d, (f) Sm 3d, (g) O 1s, and (h) C 1s.

### 4.8 Raman Spectroscopic Analysis

The Raman spectra of pristine $YVO_4$, $ZnWO_4$, and the $Sm^{3+}/ZnWO_4/YVO_4$ composite were recorded in the range of 100–1000 $cm^{-1}$ to investigate the vibrational characteristics and structural integrity of the constituent phases. As shown in Fig. 8, both the individual materials and the composite exhibit distinct Raman-active vibrational bands, confirming the presence of the characteristic metal–oxygen and polyatomic anion vibrations associated with $YVO_4$ and $ZnWO_4$. For $YVO_4$, prominent Raman bands are observed at approximately 145, 398, and 867 $cm^{-1}$. The bands in the lower- and intermediate-frequency regions can be associated mainly with lattice vibrations and bending modes of the $VO_4^{3-}$ units, whereas the strong high-frequency band around 867 $cm^{-1}$ is characteristic of the stretching vibration of the $VO_4^{3-}$ tetrahedral group[40]. These vibrational features are consistent with the tetragonal zircon-type structure of $YVO_4$. The Raman spectrum of $ZnWO_4$ exhibits characteristic bands, with a prominent feature around 332 $cm^{-1}$ and another strong band near 707 $cm^{-1}$. The lower-frequency modes are related predominantly to lattice vibrations involving Zn–O/W–O framework motions, while the high-frequency band around 707 $cm^{-1}$ is associated with vibrations of the $WO_6$ octahedral units, particularly W–O stretching[41]. The presence of these characteristic modes confirms the formation of the $ZnWO_4$ phase. The $Sm^{3+}/ZnWO_4/YVO_4$ composite retains the characteristic vibrational signatures of both $ZnWO_4$ and $YVO_4$, with bands located near 145, 332, 398, 707, and 867 $cm^{-1}$. The simultaneous observation of these modes provides evidence for the coexistence of the two oxide phases within the composite. Compared with the corresponding pristine materials, slight changes in Raman-band intensity and/or position may arise from interfacial interactions between $ZnWO_4$ and $YVO_4$ and from the incorporation of $Sm^{3+}$ ions into the composite lattice[42]. Such changes can be attributed to local structural distortion, modified metal–oxygen bonding environments, and changes in lattice symmetry induced by $Sm^{3+}$ incorporation. Importantly, no additional intense Raman bands attributable to an unwanted crystalline impurity phase are evident in the composite spectrum. Therefore, the Raman results support the successful formation of the $Sm^{3+}/ZnWO_4/YVO_4$ heterostructure and are consistent with the structural information obtained from XRD analysis.

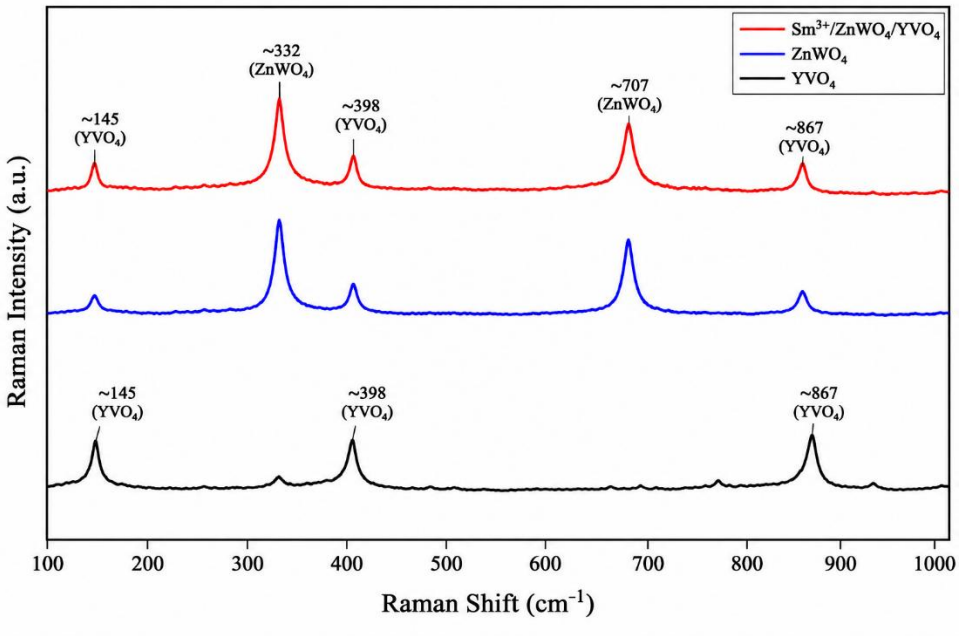



Figure 8. Raman spectroscopic analysis of $YVO_4$, $ZnWO_4$, and $Sm^{3+}/ZnWO_4/YVO_4$ heterostructure showing the characteristic vibrational modes of the constituent phases.

### 4.9 Photoluminescence analysis

The photoluminescence spectra of $ZnWO_4/YVO_4$ and $Sm^{3+}$-modified $ZnWO_4/YVO_4$ are presented in Fig. 9. $ZnWO_4/YVO_4$ exhibits a broad blue emission centered at approximately 460 nm, which can be associated with the intrinsic emission of the $ZnWO_4$ host and defect/charge-transfer states involving the $WO_6$ octahedral units. Following $Sm^{3+}$ incorporation, additional sharp emission bands appear at approximately 569, 612 and 653 nm. These emissions are assigned to the characteristic $^4G_{5/2} \rightarrow {}^6H_{5/2}$, $^4G_{5/2} \rightarrow {}^6H_{7/2}$ and $^4G_{5/2} \rightarrow {}^6H_{9/2}$ transitions of $Sm^{3+}$, respectively[43]. The emergence of these characteristic $Sm^{3+}$ emissions confirm the successful incorporation of optically active $Sm^{3+}$ centers into the $ZnWO_4/YVO_4$ host Fig. 9(a). The modification of the host PL intensity after $Sm^{3+}$ incorporation is also indicative of changes in the radiative recombination pathways and local electronic structure of the heterostructure.

The excitation spectra of $ZnWO_4/YVO_4$ and $Sm^{3+}$-modified $ZnWO_4/YVO_4$ were recorded by monitoring the emission at 612 nm, corresponding to the characteristic $^4G_{5/2} \rightarrow {}^6H_{7/2}$ transition of $Sm^{3+}$ Fig 9. (b). The $ZnWO_4/YVO_4$ heterostructure exhibits a broad excitation band in the

near-UV region, which can be attributed mainly to excitation of the host lattice and charge-transfer processes associated with the metal–oxygen framework[44]. In comparison, the $Sm^{3+}$-modified sample exhibits enhanced and more structured excitation features in the UV region, arising from the characteristic 4f–4f transitions of $Sm^{3+}$ ions. The efficient excitation of $Sm^{3+}$ centers followed by population of the $^4G_{5/2}$ excited level gives rise to the characteristic visible emissions at approximately 569, 612 and 653 nm. These results confirm the optical activation of $Sm^{3+}$ centers within the $ZnWO_4/YVO_4$ host and indicate effective interaction between the host lattice and $Sm^{3+}$ ions. The CIE 1931 chromaticity diagram was employed to evaluate the emission color characteristics of the $ZnWO_4/YVO_4$ and $Sm^{3+}$-modified $ZnWO_4/YVO_4$ samples. The $ZnWO_4/YVO_4$ sample exhibits a chromaticity coordinate of approximately (x, y) = (0.32, 0.14), corresponding to the blue-violet region and consistent with the dominant broad emission of the $ZnWO_4$ host Fig 9. (c). Upon $Sm^{3+}$ incorporation, the chromaticity coordinate shifts toward approximately (x, y) = (0.36, 0.17)[45]. This shift toward the orange-red region can be attributed to the additional characteristic $Sm^{3+}$ emissions arising from the $^4G_{5/2} \rightarrow {}^6H_{5/2}$ (~569 nm), $^4G_{5/2} \rightarrow {}^6H_{7/2}$ (~612 nm), and $^4G_{5/2} \rightarrow {}^6H_{9/2}$ (~653 nm) transitions. Thus, $Sm^{3+}$ modification effectively alters the emission color of the $ZnWO_4/YVO_4$ heterostructure[46]. The TRPL decay curves of $ZnWO_4/YVO_4$ and $Sm^{3+}$-modified $ZnWO_4/YVO_4$ were fitted using a first-order exponential decay function. The $ZnWO_4/YVO_4$ sample exhibits a decay lifetime of 3.12 ms with a decay rate of 0.321 $ms^{-1}$ and an excellent fitting coefficient ($R^2$ = 0.9987). Following $Sm^{3+}$ incorporation, the lifetime increases to 5.78 ms, while the decay rate decreases to 0.173 $ms^{-1}$ ($R^2$ = 0.9991). The prolonged lifetime indicates modification of the excited-state relaxation pathways and suggests that $Sm^{3+}$ incorporation can retard the recombination/relaxation of photoexcited carriers[5]. This prolonged excited-state lifetime is favorable for facilitating charge-transfer processes and improving the availability of photogenerated carriers for photocatalytic reactions Fig 9. (d).

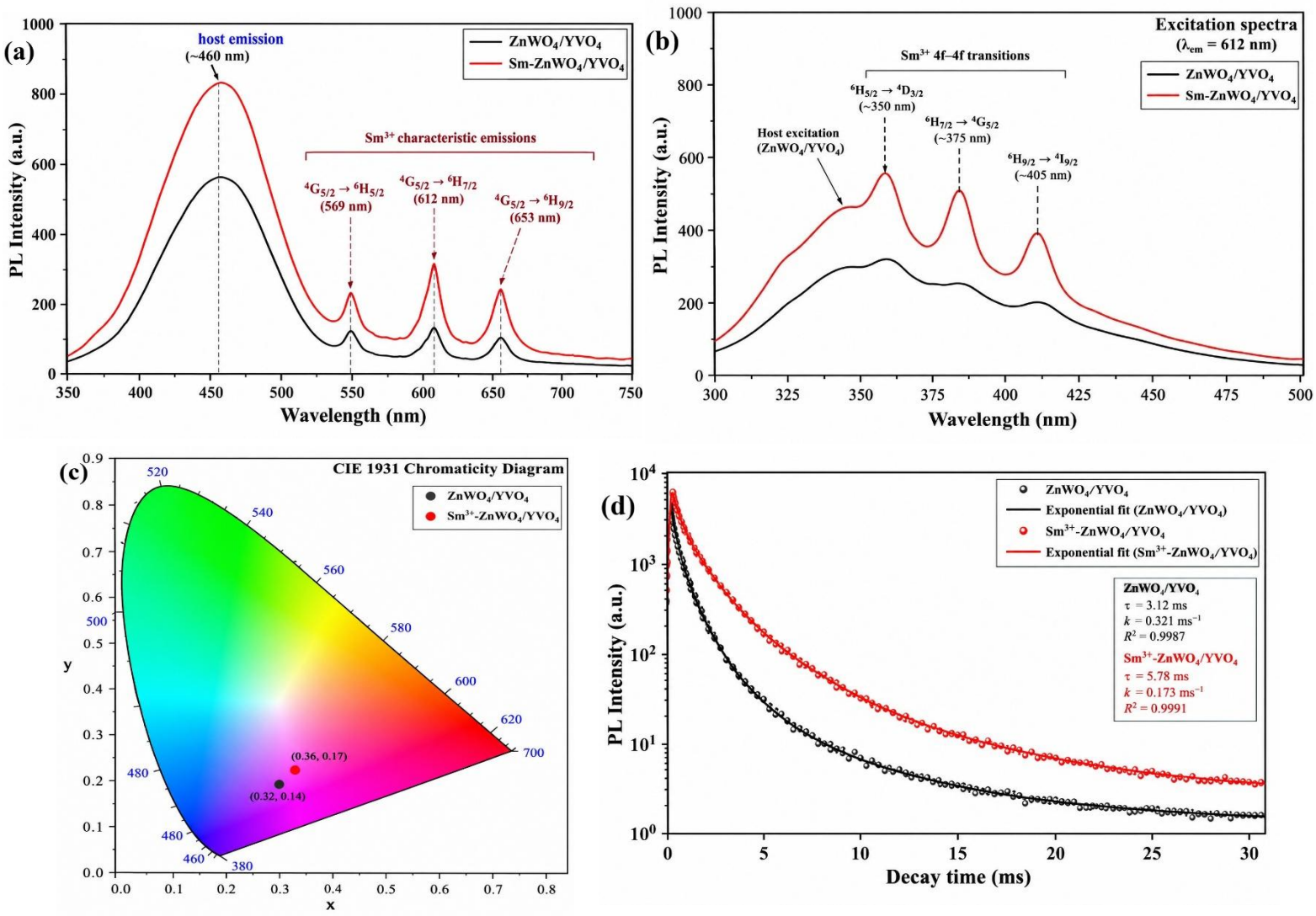



Figure 9. (a) Photoluminescence emission spectra of $ZnWO_4/YVO_4$ and $Sm^{3+}$-modified $ZnWO_4/YVO_4$; (b) photoluminescence excitation spectra monitored at $\lambda_{em}$ = 612 nm; (c) corresponding CIE 1931 chromaticity diagrams; and (d) time-resolved photoluminescence (TRPL) decay curves and exponential fitting of $ZnWO_4/YVO_4$ and $Sm^{3+}$-modified $ZnWO_4/YVO_4$.

### 4.10 UV–Vis absorbance

The UV–Vis absorption spectra of $ZnWO_4/YVO_4$ and $Sm^{3+}$-$ZnWO_4/YVO_4$ are shown in Fig. 10 (a). Both samples exhibit strong absorption in the near-UV region (approximately 250–400 nm), indicating that the $ZnWO_4/YVO_4$ heterostructure strongly interacts with high-energy photons. For $ZnWO_4/YVO_4$, the absorbance decreases rapidly after approximately 350–400 nm, followed by relatively weak absorption in the visible region. This UV absorption is mainly associated with electronic transitions involving the metal–oxygen framework, particularly O 2p → W 5d and O 2p → V 3d charge-transfer transitions. After $Sm^{3+}$ modification, the red curve shows higher absorption intensity and a broader absorption tail extending toward longer wavelengths. In particular, the $Sm^{3+}$-modified material maintains appreciable absorption beyond 400 nm and exhibits a more pronounced tail throughout the visible region. This change indicates that $Sm^{3+}$ modification alters the electronic environment of the $ZnWO_4/YVO_4$ heterostructure. The presence of $Sm^{3+}$ can introduce localized 4f-related electronic states, while $Sm^{3+}$ incorporation may also induce lattice distortion and defect-associated states. These additional electronic states can provide energetically accessible transitions and consequently extend the optical response toward longer wavelengths[47].

Fig. 10(b) presents the Tauc plots used to determine the optical band-gap energies of the pristine $ZnWO_4/YVO_4$ heterostructure and $Sm^{3+}$-modified $ZnWO_4/YVO_4$. Assuming a direct allowed electronic transition, the optical band gap was estimated using the Tauc relationship equation 2[2]:

$$(\alpha hv)^2 = A(hv - E_g) \qquad (2)$$

where α is the absorption coefficient, hv is the photon energy, A is a proportionality constant, and $E_g$ is the optical band-gap energy. The pristine $ZnWO_4/YVO_4$ exhibits an optical band gap of approximately 3.05 eV, whereas the $Sm^{3+}$-modified $ZnWO_4/YVO_4$ shows a reduced band gap of 2.87 eV[48]. Thus, $Sm^{3+}$ modification produces an apparent band-gap reduction of 0.18 eV, corresponding to approximately 5.9% relative to the pristine heterostructure. The corresponding absorption-edge wavelengths, estimated using $\boldsymbol{\lambda}$=1240/$E_g$, are approximately 406 nm for $ZnWO_4/YVO_4$ and 432 nm for $Sm^{3+}$-modified $ZnWO_4/YVO_4$, confirming the red shift of the absorption edge toward longer wavelengths. As illustrated in Fig. 10(b), the decrease in the effective optical band gap indicates that $Sm^{3+}$ incorporation modifies the electronic structure of the heterostructure. This behavior may be associated with the introduction of localized $Sm^{3+}$ 4f electronic states, defect-related energy levels arising from

lattice distortion and charge compensation, and modification of the interfacial electronic environment between $ZnWO_4$ and $YVO_4$. The enhanced electronic interaction between the constituent phases may further contribute to the observed optical response. However, the observed decrease is more appropriately described as a reduction in the effective optical band gap rather than a definitive shift of the fundamental conduction- and valence-band edges. The reduced effective band gap and red-shifted absorption edge are beneficial for photocatalytic applications because they enable the material to utilize relatively lower-energy, longer-wavelength photons more effectively.

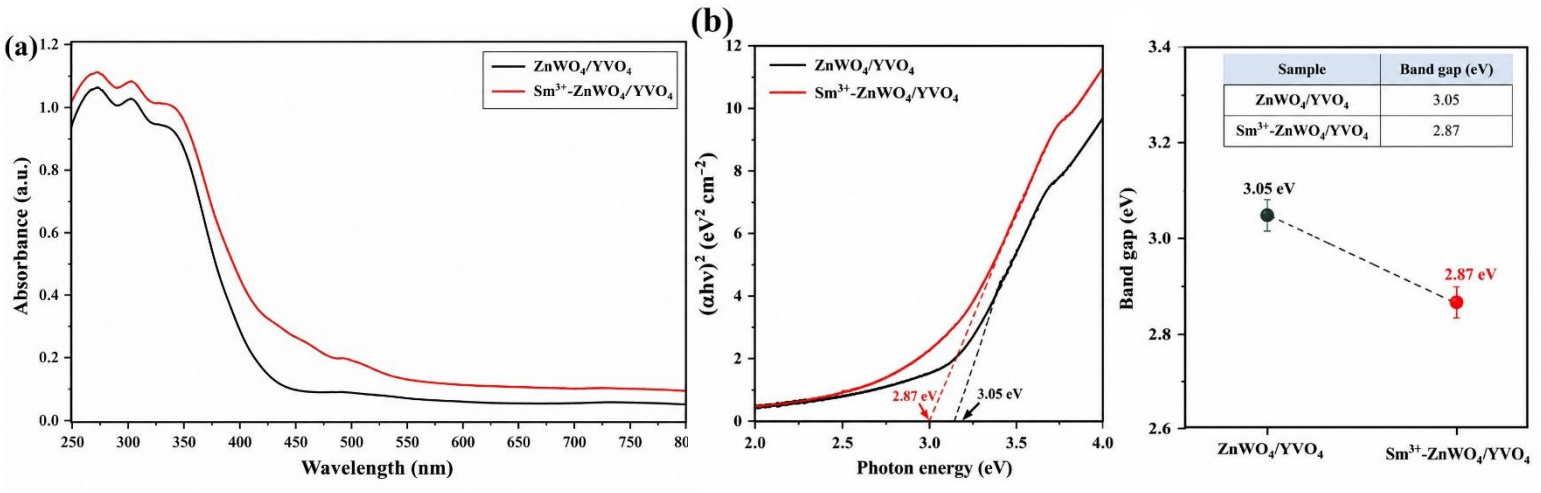



Figure 10. UV–Vis absorption spectra and optical band-gap analysis of $ZnWO_4/YVO_4$ and $Sm^{3+}$-modified $ZnWO_4/YVO_4$: (a) UV–Vis absorbance spectra, (b) Tauc plots for optical band-gap determination, and comparison of the estimated optical band-gap energies.

### 4.11 Mott–Schottky Analysis

The Mott–Schottky analysis was carried out to elucidate the semiconductor characteristics and interfacial charge-transfer properties of $ZnWO_4/YVO_4$ and $Sm^{3+}$-modified $ZnWO_4/YVO_4$. Fig 11 presents the plots of $1/C^2$ as a function of the applied potential. Both samples exhibit positive slopes in the linear regions, confirming their n-type semiconductor character, where electrons are the dominant charge carriers[49]. The positive slope is consistent with the expected behavior of n-type metal-oxide/vanadate semiconductor systems. The flat-band potential was estimated from the intercept of the linear region with the potential axis. The $ZnWO_4/YVO_4$ sample exhibits an $E_{FB}$ of approximately −0.52 V, whereas $Sm^{3+}$-$ZnWO_4/YVO_4$ shows a slightly shifted value of approximately −0.46 V versus Ag/AgCl. The observed shift in the flat-band

potential following $Sm^{3+}$ incorporation suggests modification of the surface electronic environment and charge distribution within the heterostructure. Such changes may originate from the interaction of $Sm^{3+}$ ions with the $ZnWO_4/YVO_4$ lattice and associated defect or charge-compensation processes[50].

The donor density calculated from the slope of the Mott–Schottky plots increases from approximately $3.21 \times 10^{19}\ cm^{-3}$ for $ZnWO_4/YVO_4$ to $4.12 \times 10^{19}\ cm^{-3}$ for $Sm^{3+}$-$ZnWO_4/YVO_4$. The increased donor density indicates a higher concentration of electrically active donor states following $Sm^{3+}$ modification. This behavior may facilitate electron transport and influence charge separation at the $ZnWO_4/YVO_4$ interface. The Mott–Schottky results therefore demonstrate that $Sm^{3+}$ modification significantly influences the electronic properties of the $ZnWO_4/YVO_4$ heterostructure[51]. The increased donor density, together with the shift in flat-band potential, suggests improved electronic interaction and modified charge-carrier distribution. These changes, combined with the reduced effective optical band gap observed from the Tauc analysis, may contribute to improved light utilization and charge-transfer characteristics of $Sm^{3+}$-$ZnWO_4/YVO_4$.

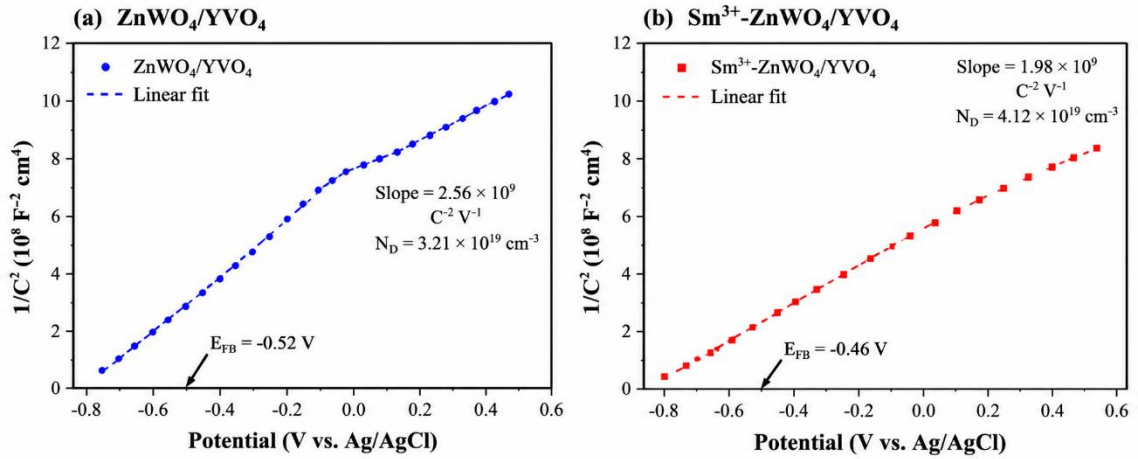



Figure 11. Mott–Schottky plots of (a) $ZnWO_4/YVO_4$ and (b) $Sm^{3+}$-$ZnWO_4/YVO_4$. The positive slopes indicate n-type semiconductor behavior, while the x-axis intercepts provide estimates of the flat-band potentials.

**Photocatalytic degradation of Crystal violet**

The photocatalytic degradation performance of the prepared catalysts was initially evaluated using Crystal Violet (CV) as a model organic dye. As shown in Fig. 12. (a), the unmodified

$ZnWO_4/YVO_4$ catalyst exhibited a degradation efficiency of approximately 78% toward Crystal Violet. In comparison, incorporation of $Sm^{3+}$ into the $ZnWO_4/YVO_4$ system significantly enhanced the photocatalytic performance, with the $Sm^{3+}/ZnWO_4/YVO_4$ composite achieving about 93% degradation under the same experimental conditions. The improved activity can be attributed to the beneficial role of $Sm^{3+}$ modification in promoting charge separation and suppressing the recombination of photogenerated electron–hole pairs, thereby increasing the availability of reactive charge carriers for the degradation reaction[32]. Based on its superior photocatalytic performance, the $Sm^{3+}$-modified $ZnWO_4/YVO_4$ composite was selected for further characterization and subsequent photocatalytic investigations. The $Sm^{3+}$-modified $ZnWO_4/YVO_4$ composite, exhibiting the highest Crystal Violet degradation efficiency (93%), was therefore selected as the optimized photocatalyst for photocatalytic studies.

As shown in Fig. 12. (b), the influence of catalyst dosage on Crystal Violet degradation was subsequently investigated. The degradation efficiency increased from approximately 45% at 5 mg $L^{-1}$ to 50% at 10 mg $L^{-1}$, and further increased to 67% at 15 mg $L^{-1}$. The maximum degradation efficiency of approximately 91% was obtained at 20 mg $L^{-1}$, indicating that this dosage provided an optimum balance between the number of available active sites and light utilization. Further increasing the catalyst concentration to 25 and 30 mg $L^{-1}$ resulted in a decrease in degradation efficiency to approximately 81% and 49%, respectively. This decline may be associated with increased light scattering/shielding and particle agglomeration at higher catalyst concentrations, which reduce effective light penetration and the availability of illuminated active sites.

As shown in Fig. 12(c), the effect of the initial Crystal Violet concentration on the photocatalytic degradation process was investigated over the concentration range of 10–50 ppm. The degradation behavior was strongly dependent on the initial dye concentration. At lower dye concentrations, a greater proportion of the dye molecules can interact with the illuminated surface of the $Sm^{3+}$-modified $ZnWO_4/YVO_4$ photocatalyst because a larger number of active sites are available relative to the number of dye molecules. With increasing initial dye concentration, the number of dye molecules competing for the available active sites increases, while the penetration of incident light through the reaction suspension can be reduced by the stronger absorption of light by the dye molecules[52]. Consequently, the generation and effective utilization of reactive species such as •OH and $\bullet O_2^-$ may be reduced at higher dye concentrations, resulting in lower degradation efficiency.

As shown in Fig. 12(d), the photocatalytic degradation of Crystal Violet (CV) by the $Sm^{3+}$-modified $ZnWO_4/YVO_4$ composite was strongly influenced by the initial pH of the solution. The degradation efficiency increased from approximately 45% at pH 1 to a maximum of about 88% at pH 3, indicating that pH 3 is the optimum condition for CV degradation. The enhanced degradation under mildly acidic conditions can be associated with favorable surface-charge characteristics of the photocatalyst, improved interaction between CV molecules and the catalyst surface, and more efficient generation and utilization of reactive oxygen species during irradiation. When the pH was further increased to 5 and 7, the degradation efficiency decreased to approximately 59% and 34%, respectively. A pronounced decrease was observed under alkaline conditions, with the degradation efficiency falling to about 12% at pH 9 and 7% at pH 11. This reduction may arise from changes in the surface charge and surface protonation state of the $ZnWO_4/YVO_4$ photocatalyst, which can influence the adsorption of the dye and the interfacial photocatalytic reactions. At higher pH, changes in the availability and lifetime of photogenerated reactive species, together with altered dye–catalyst interactions, may further suppress the degradation process. Thus, pH 3 was identified as the optimum pH, providing the highest CV degradation efficiency (~88%). The strong dependence of photocatalytic activity on pH highlights the importance of solution acidity in controlling the surface interactions and charge-transfer processes involved in Crystal Violet degradation.

The time-dependent UV–visible absorption spectra of Crystal Violet (CV) are presented in Fig. 12(e). The characteristic absorption band of CV is observed at approximately 590 nm. With increasing irradiation time from 0 to 90 min, the intensity of this absorption peak progressively decreases, demonstrating the continuous removal of CV from the aqueous solution during photocatalytic treatment. The gradual decrease in absorbance indicates a reduction in the dye concentration in the presence of the $Sm^{3+}$-modified $ZnWO_4/YVO_4$ photocatalyst. The photocatalytic degradation efficiency was calculated using the following equation (3)[53]:

$$Degradation\ \% = \frac{C_0 - C_t}{C_0} \times 100 \quad (3)$$

where $C_0$ is the initial concentration of crystal violet and $C_t$ is the concentration of dye at irradiation time 't'. The degradation efficiency after 90 min of irradiation was calculated to be approximately 93%. Thus, the pronounced decrease in the characteristic absorption band, together with the calculated degradation efficiency, confirms the excellent photocatalytic activity of the $Sm^{3+}$-modified $ZnWO_4/YVO_4$ composite toward Crystal Violet.

The photocatalytic degradation kinetics of Crystal Violet were evaluated using the pseudo-first-order kinetic model equation 4:

$$\ln\left(\frac{C_0}{C_t}\right) = k_{app}t \quad (4)$$

where $C_0$ is the initial concentration of Crystal Violet, $C_t$ is its concentration at irradiation time t, and $k_{app}$ is the apparent first-order rate constant. As shown in Fig. 12(f), a nearly linear relationship was obtained between$\ln\left(\frac{C_0}{C_t}\right)$ and irradiation time, with a high correlation coefficient of $R^2$ = 0.992. The excellent linearity and high $R^2$ value indicate that the photocatalytic degradation of Crystal Violet closely follows pseudo-first-order kinetics under the investigated experimental conditions. The slope of the linear regression corresponds to the apparent rate constant $k_{app}$ , while the high $R^2$ value confirms the good agreement of the experimental data with the pseudo-first-order kinetic model. These results demonstrate that the degradation rate is approximately proportional to the instantaneous concentration of Crystal Violet during the photocatalytic reaction.

The proposed photocatalytic mechanism for Crystal Violet (CV) degradation over the $Sm^{3+}$-modified $ZnWO_4/YVO_4$ heterostructure is illustrated in Fig. 12(g) Upon light irradiation, the $ZnWO_4/YVO_4$ heterostructure absorbs photons and generates photogenerated electron–hole pairs. The formation of an intimate interface between $ZnWO_4$ and $YVO_4$ promotes interfacial charge transfer and suppresses the recombination of photogenerated carriers. The incorporation of $Sm^{3+}$ ions further facilitate charge separation by providing additional charge-transfer/trapping sites, thereby increasing the lifetime and availability of photogenerated electrons and holes. The photogenerated electrons participate in the reduction of dissolved oxygen to generate superoxide radical anions according to equation 5:

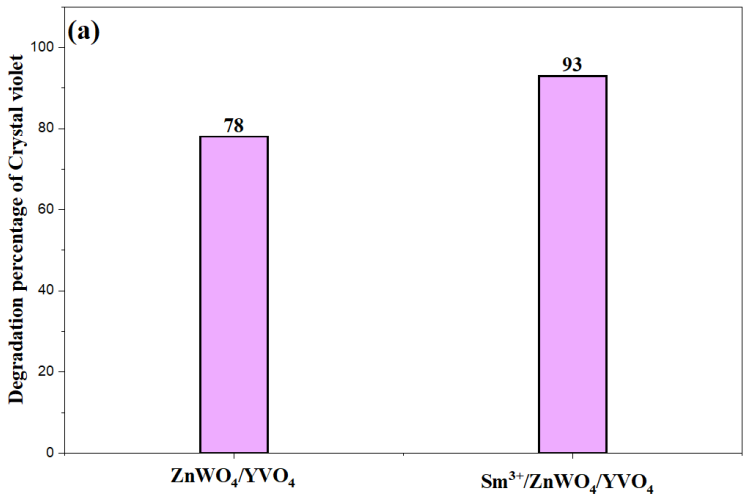
$$O_2 + e^- \rightarrow \cdot O_2 - \quad (5)$$

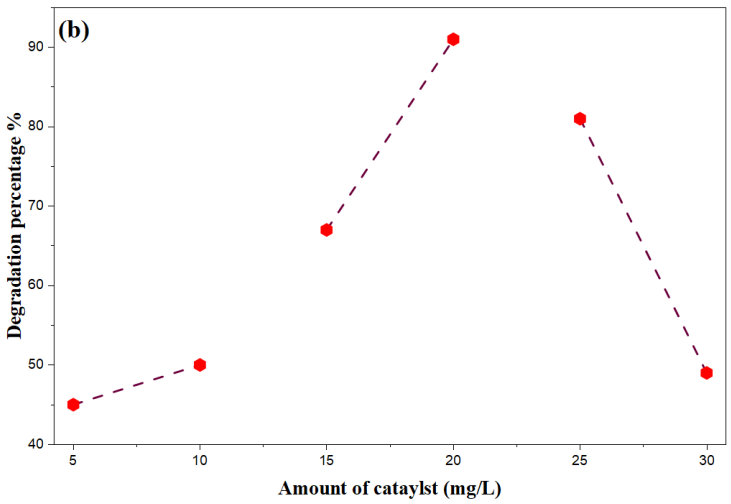
Meanwhile, the photogenerated holes react with surface-adsorbed water or hydroxide ions to produce highly reactive hydroxyl radicals' equation 6:

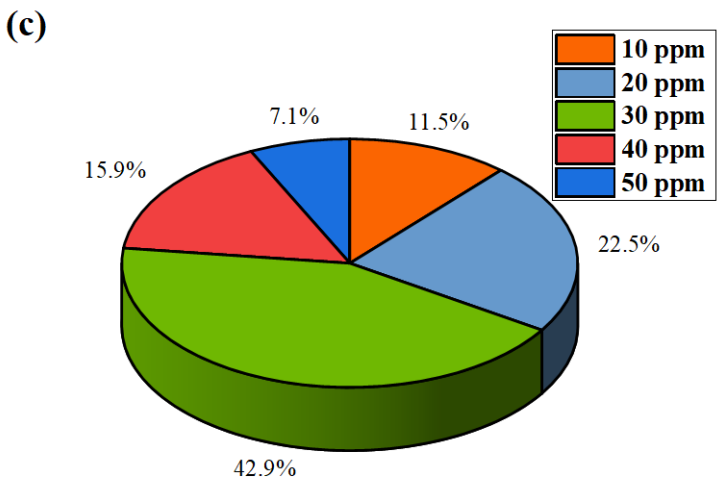
$$\left.\begin{aligned} h^+ + H_2O &\rightarrow \cdot OH + H^+ \\ h^+ + OH^- &\rightarrow \cdot OH \end{aligned}\right\} \quad (6)$$

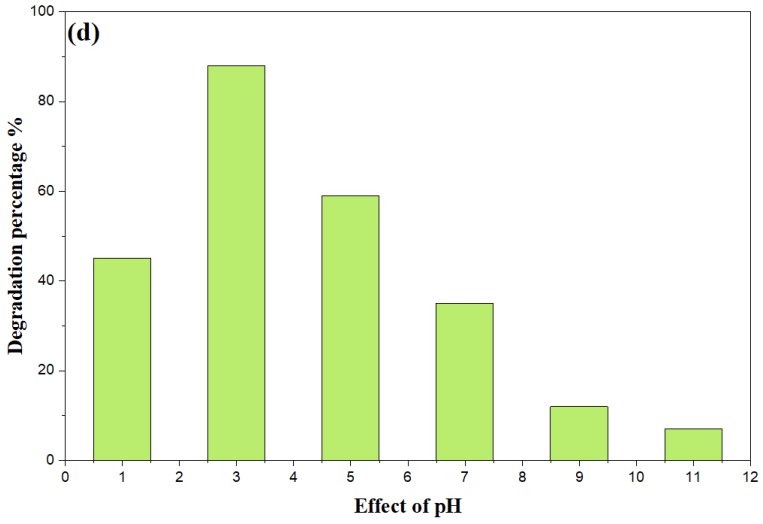
The generated $\cdot O_2 -$ and $\cdot OH$ together with the photogenerated holes, contribute to the oxidative degradation of CV. These reactive species attack the conjugated chromophoric structure of CV,

resulting in the disruption of its molecular structure through successive oxidation and N-dealkylation reactions. Consequently, CV is transformed into a series of smaller organic intermediates, which undergo further oxidation and fragmentation. Continued photocatalytic oxidation can ultimately lead to the formation of low-molecular-weight products and, under sufficiently complete degradation conditions, mineralization into $CO_2$, $H_2O$, and inorganic species. Overall, the enhanced photocatalytic performance of the $Sm^{3+}$-modified $ZnWO_4/YVO_4$ heterostructure can be attributed to improved light absorption, efficient interfacial charge separation, suppressed electron–hole recombination, and enhanced generation of reactive oxygen species. These synergistic effects promote the efficient degradation of Crystal Violet under light irradiation.



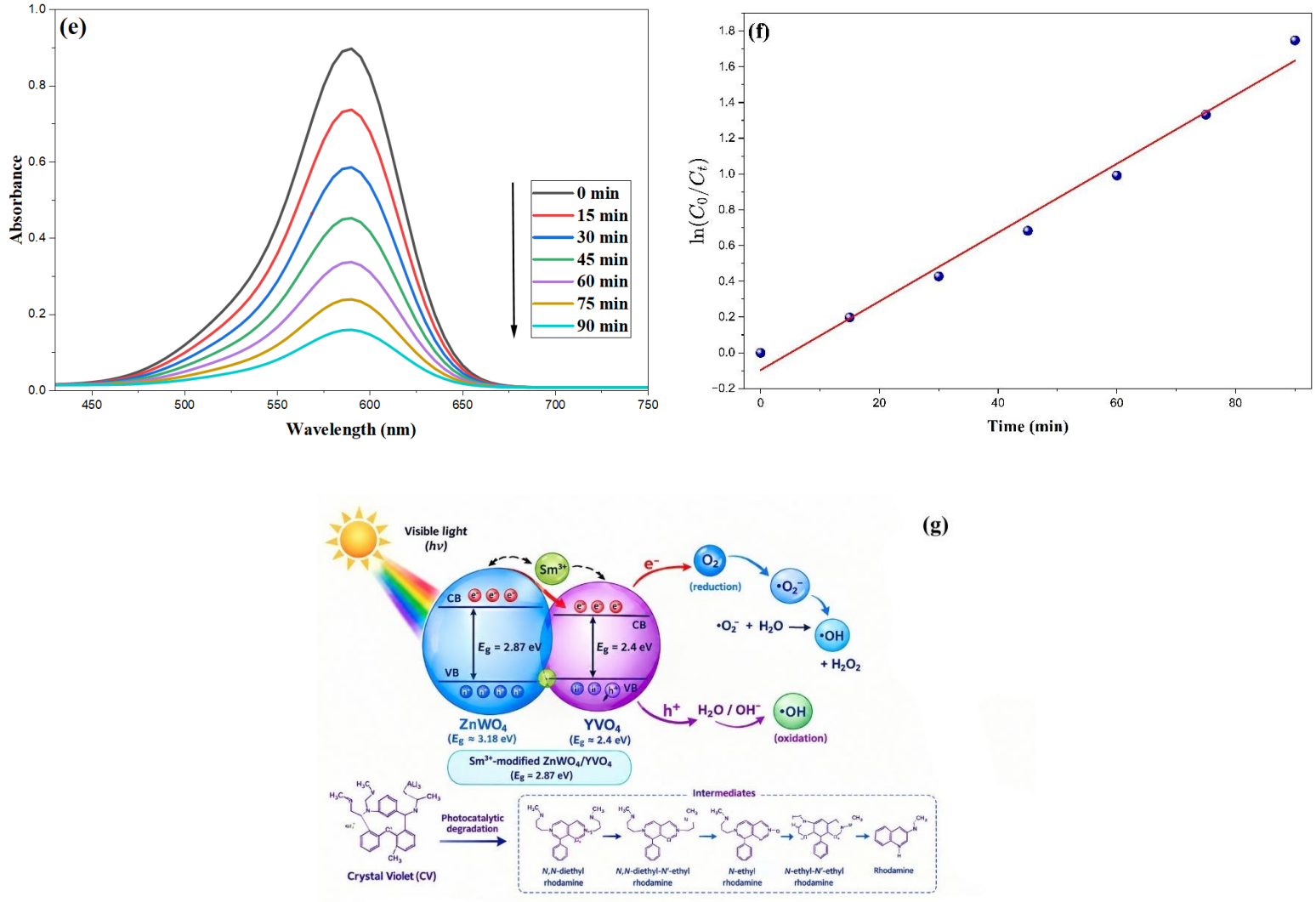



Figure 12. (a) Comparison of Crystal Violet degradation by pristine $ZnWO_4/YVO_4$ and $Sm^{3+}$-modified $ZnWO_4/YVO_4$ catalysts, (b) effect of catalyst dosage, (c) effect of initial dye concentration, (d) effect of solution pH, (e) time-dependent UV–visible absorption spectra, and (f) pseudo-first-order kinetic plot. (g) Proposed photocatalytic mechanism of $Sm^{3+}$-modified $ZnWO_4/YVO_4$ heterostructure for the degradation of Crystal Violet under light irradiation.

### 4.13 Photocatalytic degradation of Sulfamethoxazole

Fig. 11(a) compares the photocatalytic degradation performance of the pristine $ZnWO_4/YVO_4$ heterostructure and $Sm^{3+}$-modified $ZnWO_4/YVO_4$ toward sulfamethoxazole (SMX). The pristine $ZnWO_4/YVO_4$ exhibited 58% degradation of SMX, whereas the incorporation of $Sm^{3+}$ substantially enhanced the degradation efficiency to 97% under otherwise identical experimental conditions. The remarkable improvement following $Sm^{3+}$ modification can be

associated with the alteration of the electronic and interfacial properties of the heterostructure. The introduction of $Sm^{3+}$ ions can act as charge-trapping or charge-transfer centers, thereby promoting the spatial separation of photogenerated electrons and holes and reducing their direct recombination. Consequently, a greater fraction of the photogenerated charge carriers can participate in surface redox reactions. The $Sm^{3+}$ species may also modify the local electronic environment and defect structure of the $ZnWO_4/YVO_4$ interface, potentially providing additional active sites for the adsorption and subsequent oxidation of SMX. The enhanced separation and utilization of photogenerated charge carriers can promote the formation of reactive oxygen species (ROS), such as hydroxyl radicals (•OH) and superoxide radicals ($•O_2^-$), depending on the band positions and reaction environment. These reactive species can attack the aromatic rings, heterocyclic moieties, and functional groups present in the SMX molecule, ultimately leading to its progressive degradation[54]. Therefore, the markedly higher degradation efficiency obtained with $Sm^{3+}/ZnWO_4/YVO_4$ demonstrates the beneficial effect of $Sm^{3+}$ modification. Based on its superior photocatalytic performance, $Sm^{3+}/ZnWO_4/YVO_4$ was selected for subsequent optimization of the catalyst dosage, initial SMX concentration, and solution pH. The influence of catalyst dosage on SMX degradation is presented in Fig. 11(b). The degradation efficiency increased progressively from 29% to 93% when the catalyst dosage was increased from 5 to 20 mg $L^{-1}$. At a low catalyst loading of 5 mg $L^{-1}$, the number of available surface-active sites and photogenerated charge carriers is comparatively limited, resulting in lower interaction between the catalyst surface and SMX molecules. Increasing the catalyst dosage provides a larger number of accessible active sites, thereby enhancing SMX adsorption and increasing the number of surface sites at which photogenerated electrons and holes can participate in redox reactions. In addition, a higher concentration of catalyst particles provides a greater number of photoactive centers capable of absorbing incident photons, which can increase the generation of reactive charge carriers and consequently improve the degradation efficiency. The increase from 5 to 20 mg $L^{-1}$ therefore indicates that the photocatalytic system benefits from the greater availability of active sites and photoinduced charge carriers within this concentration range. However, a further increase in catalyst loading resulted in a decrease in degradation efficiency, with 77% and 51% degradation obtained at 25 and 30 mg $L^{-1}$, respectively. Although increasing the catalyst concentration initially provides additional active sites, excessive catalyst loading can cause increased turbidity of the suspension, particle aggregation, and enhanced scattering and shielding of the incident irradiation. As a result, the effective penetration of light into the reaction suspension can be reduced, preventing a proportion of the catalyst particles from being efficiently irradiated.

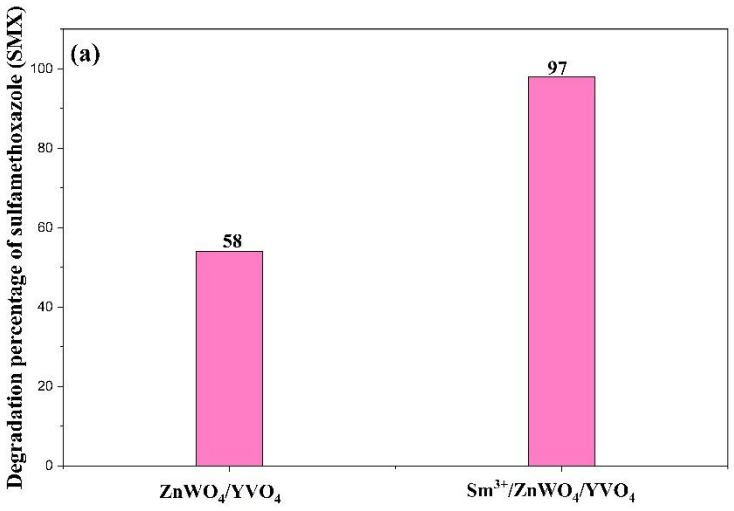
Particle aggregation can additionally decrease the effective surface area available for interaction with SMX and may reduce the accessibility of active sites. At excessively high catalyst concentrations, therefore, the increase in the total number of catalyst particles does not necessarily result in a proportional increase in photocatalytic activity. The decrease observed beyond 20 mg $L^{-1}$ suggests that an optimum balance exists between the availability of active sites and efficient light penetration. Accordingly, 20 mg $L^{-1}$ was selected as the optimum catalyst dosage for the subsequent experiments. The effect of the initial SMX concentration on the photocatalytic degradation process is shown in Fig. 11(c). The degradation efficiency increased from 41% at 10 ppm to 81% at 40 ppm, followed by a pronounced decrease to 54% at 50 ppm. The increase observed at relatively low SMX concentrations can be related to the interaction between the pollutant molecules and the available active sites of the $Sm^{3+}/ZnWO_4/YVO_4$ photocatalyst. At lower concentrations, a sufficient number of active sites are available relative to the number of SMX molecules, allowing efficient adsorption and subsequent attack by photogenerated reactive species. As the concentration increases, the probability of collision between SMX molecules and the catalyst surface also increases, which can initially favor the photocatalytic reaction. The maximum degradation at 40 ppm indicates that the catalyst provides a favorable balance between the available SMX molecules, surface-active sites, and generated reactive species under the investigated conditions. However, when the initial concentration was further increased to 50 ppm, the degradation efficiency decreased considerably. At higher pollutant concentrations, the number of SMX molecules becomes relatively high compared with the available photocatalytically active sites and reactive species. Consequently, competition among SMX molecules for adsorption and reaction sites can occur, resulting in incomplete utilization of the catalyst surface. Furthermore, a higher concentration of SMX can increase the absorption of incident radiation by the pollutant molecules themselves, thereby decreasing the amount of light reaching the catalyst surface. This so-called inner-filter or light-screening effect can reduce the generation of electron–hole pairs and consequently decrease the production of reactive species. Accumulation of SMX and its intermediate products on the catalyst surface may also partially block active sites and inhibit further reaction. Thus, the decrease at 50 ppm can be attributed to the combined effects of limited active sites, competition for reactive species, and reduced light penetration. Based on the maximum degradation obtained, 40 ppm was selected as the optimum initial SMX concentration.

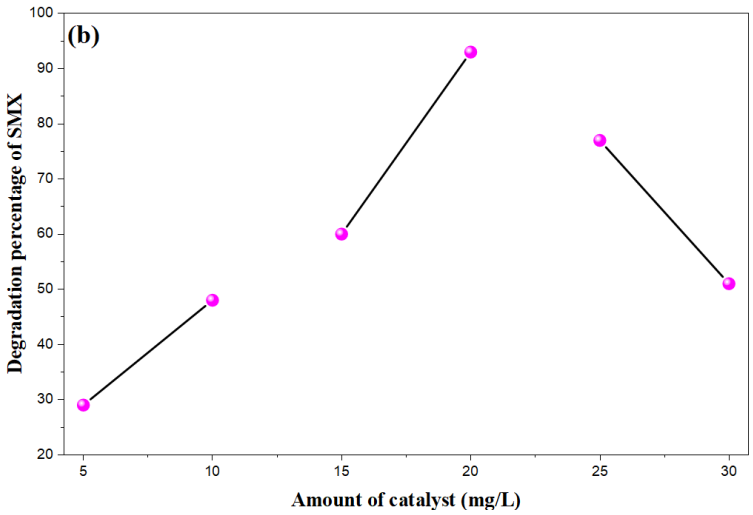
The effect of solution pH on SMX degradation is presented in Fig. 11(d). The photocatalytic degradation was strongly dependent on the reaction pH, increasing from 66% at pH 1 to a maximum of 89% at pH 5, followed by a gradual decrease to 34% at pH 11. The dependence of photocatalytic activity on pH can be associated with changes in the surface charge of the photocatalyst, the ionization state of SMX, the adsorption behavior of the pollutant, and the formation and reactivity of ROS. SMX is a weakly ionizable pharmaceutical compound containing functional groups that undergo protonation/deprotonation depending on the solution pH. Consequently, its molecular form and interaction with the catalyst surface change with pH. Under acidic conditions, protonation of surface functional groups and SMX can influence adsorption and the interfacial transfer of photogenerated charge carriers. As the pH increased toward pH 5, more favorable surface–pollutant interactions may have facilitated the adsorption of SMX and its subsequent reaction with photogenerated reactive species, resulting in the highest degradation efficiency of 89%. In addition, the solution pH can influence the generation and lifetime of hydroxyl radicals and other reactive oxygen species involved in the degradation process. At strongly alkaline conditions, the decline in degradation efficiency can result from changes in the ionization state of SMX and the surface charge of the catalyst, which may decrease the effective adsorption of SMX onto the catalyst surface. Electrostatic repulsion between similarly charged species may further hinder close contact between SMX and the photocatalyst. Moreover, the abundance of hydroxide ions at high pH can alter the relative contribution and reaction pathways of different ROS[55]. The pronounced decrease to 34% at pH 11 therefore indicates that strongly alkaline conditions are unfavorable for the photocatalytic degradation of SMX in the present system. Overall, pH 5 provided the most favorable conditions for SMX degradation and was therefore selected as the optimum reaction pH.

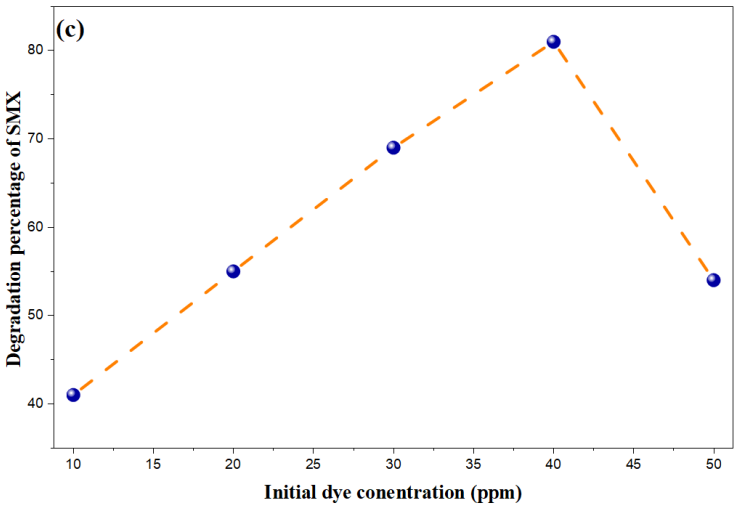
Fig. 11(e) shows the UV–visible absorption spectra of SMX recorded at different irradiation times during photocatalytic degradation using $Sm^{3+}/ZnWO_4/YVO_4$. The absorption intensity progressively decreased with increasing irradiation time, confirming the gradual degradation of SMX. The characteristic absorption band of SMX in the UV region showed a continuous decrease from the initial spectrum (0 min) to 90 min, indicating the breakdown of the parent SMX molecule and its transformation into intermediate products. After 90 min of irradiation, approximately 97% degradation of SMX was achieved, demonstrating the high photocatalytic efficiency of the $Sm^{3+}/ZnWO_4/YVO_4$ heterostructure. The continuous decrease in absorbance without the appearance of a significant new absorption band further suggests the progressive destruction of the parent pollutant rather than simple spectral shifting. The photocatalytic

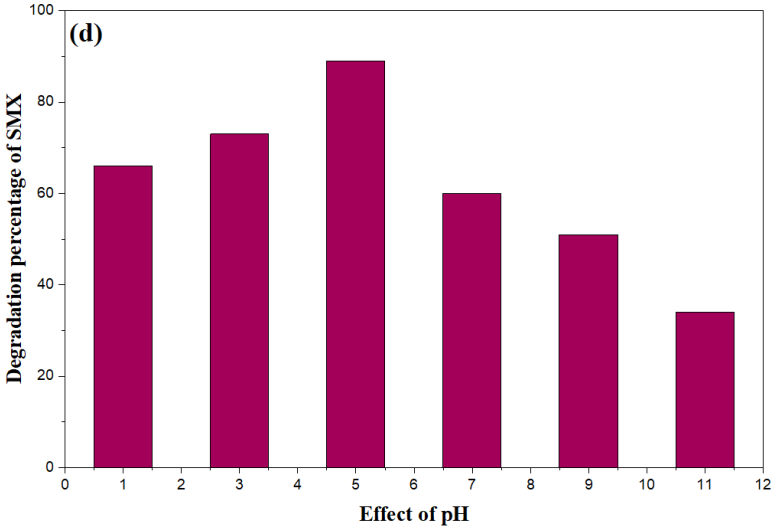
degradation kinetics of SMX were further evaluated using the pseudo-first-order kinetic model, as shown in Fig. 11(f). The linear relationship between $\ln(C_0/C_t)$ and irradiation time indicates that the degradation process follows pseudo-first-order kinetics. The corresponding linear regression exhibited a coefficient of determination ($R^2$) of 0.981, demonstrating a good correlation between the experimental data and the pseudo-first-order kinetic model. The high $R^2$ value confirms that the degradation rate is reasonably well described by pseudo-first-order kinetics under the investigated experimental conditions. The obtained kinetic behavior, together with the 97% degradation efficiency, confirms the effective photocatalytic activity of $Sm^{3+}/ZnWO_4/YVO_4$ toward SMX degradation.

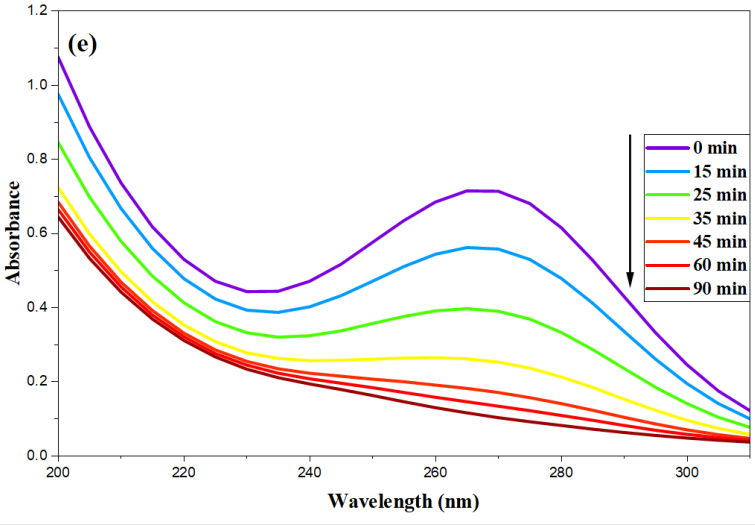
The proposed photocatalytic degradation mechanism of sulfamethoxazole (SMX) over the $Sm^{3+}$-modified $ZnWO_4/YVO_4$ heterostructure is illustrated in Fig. 11(g). Under visible-light irradiation, the heterostructure absorbs photons and generates photogenerated electron–hole pairs. The formation of the $ZnWO_4/YVO_4$ heterointerface facilitates interfacial charge separation and transfer, thereby suppressing the rapid recombination of photogenerated electrons and holes. The incorporated $Sm^{3+}$ ions may additionally act as charge-trapping or transfer centers, contributing to improved carrier separation. The photogenerated conduction-band electrons react with dissolved oxygen molecules to generate superoxide radicals whereas the photogenerated valence-band holes react with surface hydroxyl groups or water molecules to generate highly reactive hydroxyl radicals. These reactive oxygen species, together with the photogenerated holes, attack the SMX molecules adsorbed on the catalyst surface. The degradation proceeds through successive oxidation reactions involving hydroxylation of the aromatic moiety, cleavage of the sulfonamide linkage, transformation and opening of the isoxazole ring, followed by cleavage of the aromatic structure into smaller oxygenated organic intermediates. With continued irradiation, these intermediates undergo further oxidation and ultimately may proceed toward mineralization, yielding $CO_2$, $H_2O$, and inorganic nitrogen- and sulfur-containing species. Thus, the enhanced photocatalytic activity of the $Sm^{3+}$-modified $ZnWO_4/YVO_4$ heterostructure can be attributed to its improved light absorption, efficient interfacial charge separation, $Sm^{3+}$-assisted charge-transfer processes, and the generation of reactive oxygen species responsible for the oxidative degradation of SMX.

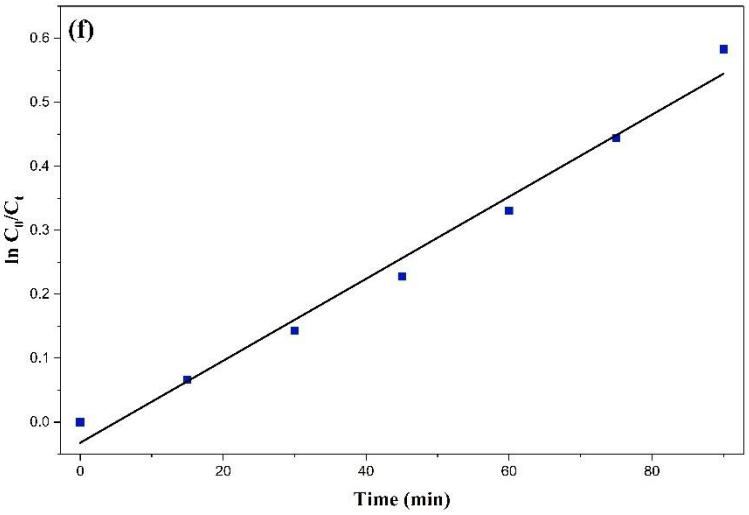

(a)
Degradation percentage of sulfamethoxazole (SMX)
58
97
ZnWO4/YVO4
Sm3+/ZnWO4/YVO4


(b)
Degradation percentage of SMX
Amount of catalyst (mg/L)


(c)
Degradation percentage of SMX
Initial dye conentration (ppm)


(d)
Degradation percentage of SMX
Effect of pH


(e)
Absorbance
Wavelength (nm)
0 min
15 min
25 min
35 min
45 min
60 min
90 min


(f)
ln C0/Ct
Time (min)

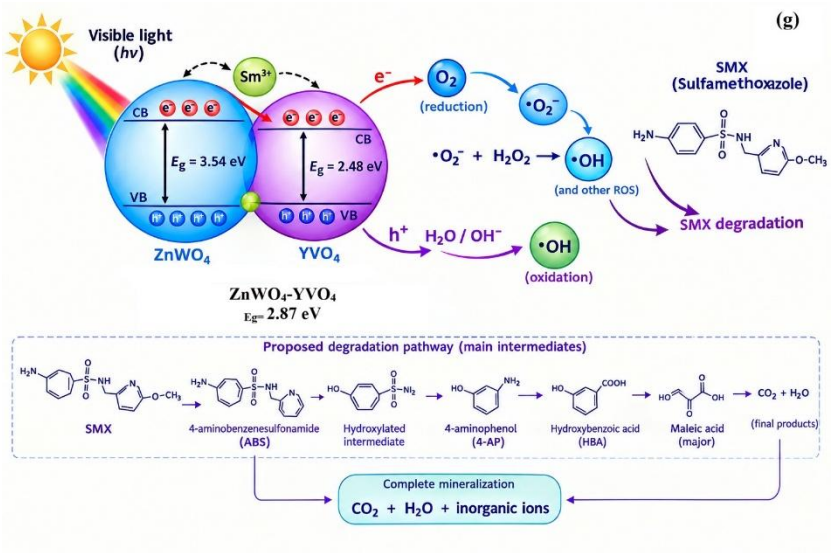



Figure 11. (a) Comparison of SMX degradation using $ZnWO_4/YVO_4$ and $Sm^{3+}/ZnWO_4/YVO_4$; (b) effect of catalyst dosage; (c) effect of initial SMX concentration; (d) effect of solution pH; (e) UV–visible absorption spectra of SMX at different irradiation times; and (f) pseudo-first-order kinetic plot for SMX degradation over $Sm^{3+}/ZnWO_4/YVO_4$. (g) Proposed mechanism for visible-light-driven photocatalytic degradation of sulfamethoxazole (SMX) over the $Sm^{3+}$-modified $ZnWO_4/YVO_4$ heterostructure.

### 4.14 Effect of Scavengers

To identify the dominant reactive species involved in the photocatalytic degradation of CV and SMX, radical-scavenging experiments were conducted using isopropanol (IPA), benzoquinone (BQ), and EDTA as scavengers for •OH, $•O_2^-$, and photogenerated $h^+$, respectively. As shown in Fig. 12, the $Sm^{3+}/ZnWO_4/YVO_4$ photocatalyst exhibited degradation efficiencies of approximately 93% and 97% toward CV and SMX, respectively, in the absence of scavengers. Upon addition of IPA, the degradation efficiencies decreased markedly to approximately 45% for CV and 39% for SMX, demonstrating the significant contribution of hydroxyl radicals to the photocatalytic oxidation process. The corresponding decrease in degradation can be attributed to the effective quenching of •OH by IPA, thereby suppressing the oxidation pathways responsible for pollutant decomposition[56]. Addition of BQ also reduced the degradation efficiencies to approximately 65% and 55% for CV and SMX, respectively, indicating the involvement of superoxide radicals ($•O_2^-$). Similarly, the presence of EDTA decreased the degradation efficiencies to approximately 67% for CV and 69% for SMX, confirming the contribution of photogenerated holes. Among the investigated scavengers, IPA produced the greatest inhibition of degradation for both pollutants, suggesting that •OH radicals play the predominant role in the photocatalytic degradation process, followed by $•O_2^-$ and $h^+$[57].

These results are consistent with the proposed ROS-mediated photocatalytic mechanism, in which photogenerated holes promote •OH formation through oxidation of surface $H_2O/OH^-$, while photogenerated electrons reduce dissolved $O_2$ to $\bullet O_2^-$. The resulting reactive species subsequently attack the molecular structures of CV and SMX, leading to their progressive oxidation and degradation.

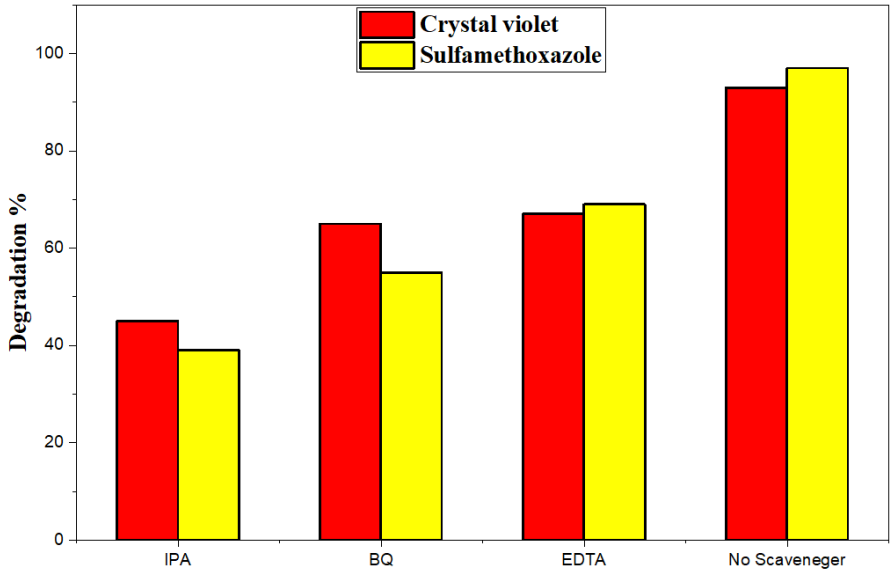



Figure 12. Effect of reactive-species scavengers on the photocatalytic degradation of Crystal Violet and sulfamethoxazole over $Sm^{3+}/ZnWO_4/YVO_4$: IPA as a $^{\bullet}OH$ scavenger, BQ as a $^{\bullet}O_2^-$ scavenger, and EDTA as a photogenerated-hole scavenger.

### 4.15 Reusability of catalyst

The reusability of the photocatalyst was evaluated over seven consecutive photocatalytic cycles for the degradation of crystal violet (CV) and sulfamethoxazole (SMX), as shown in Fig. 13(a). The catalyst exhibited excellent stability and retained a high photocatalytic efficiency throughout the repeated cycles. For CV, the degradation efficiency gradually decreased from approximately 93% in the first cycle to 87% in the seventh cycle, while the degradation of SMX decreased from approximately 97% to 89% over the same seven cycles. The relatively small decrease in degradation efficiency indicates that the active photocatalytic sites of the catalyst remain largely preserved after repeated use[58]. The slight loss in activity may be attributed to the adsorption of residual dye/pollutant molecules or their degradation intermediates on the catalyst surface, partial occupation of active sites, and minor loss of catalyst during the recovery and washing steps. The SEM image in Fig. 13(b) further shows

that the catalyst retains its characteristic rod-like morphology after repeated photocatalytic operation, indicating good structural stability[59]. Overall, the high degradation efficiency maintained over seven successive cycles, together with the preserved morphology, demonstrates the good reusability and structural stability of the catalyst, highlighting its potential for repeated treatment of CV- and SMX-contaminated water.

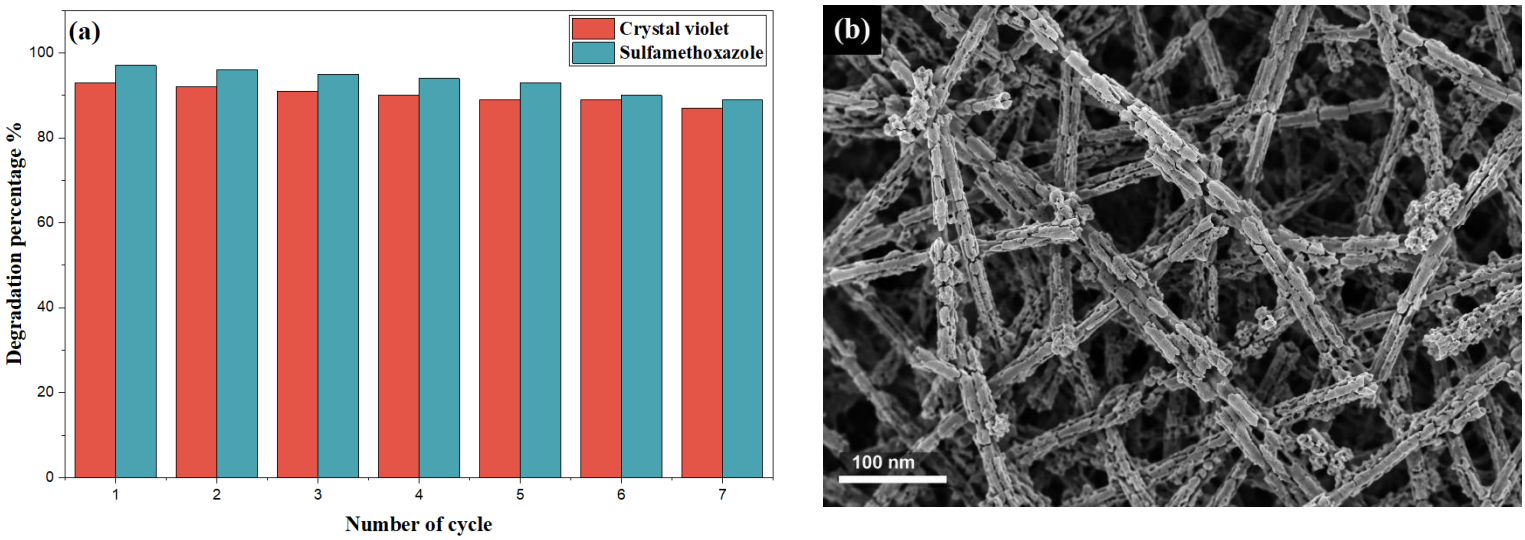



Figure 13. Reusability and structural stability of the photocatalyst over seven consecutive photocatalytic cycles for CV and SMX degradation: (a) degradation efficiency after each cycle and (b) SEM image of the recovered catalyst after repeated use.

### 4.16 EIS analysis

The EIS Nyquist plots were used to investigate the charge-transfer properties of the synthesized photocatalysts given in Fig. 14. The $Sm^{3+}$-modified $ZnWO_4/YVO_4$ heterostructure exhibits the smallest semicircular diameter compared with pristine $ZnWO_4$ and $YVO_4$, indicating the lowest interfacial charge-transfer resistance. The estimated Rct values decrease from approximately 780 Ω for $ZnWO_4$ and 520 Ω for $YVO_4$ to 260 Ω for the $Sm^{3+}$-modified $ZnWO_4/YVO_4$ heterostructure. The reduced charge-transfer resistance demonstrates facilitated migration and separation of photogenerated charge carriers at the heterointerface[60]. The improved charge-transfer kinetics can be attributed to the intimate $ZnWO_4/YVO_4$ interface and the charge-trapping/transfer role of $Sm^{3+}$ species, which suppress electron–hole recombination[61]. These results support the enhanced availability of photogenerated carriers for surface redox reactions

and reactive oxygen species generation, thereby contributing to the superior photocatalytic degradation of SMX.

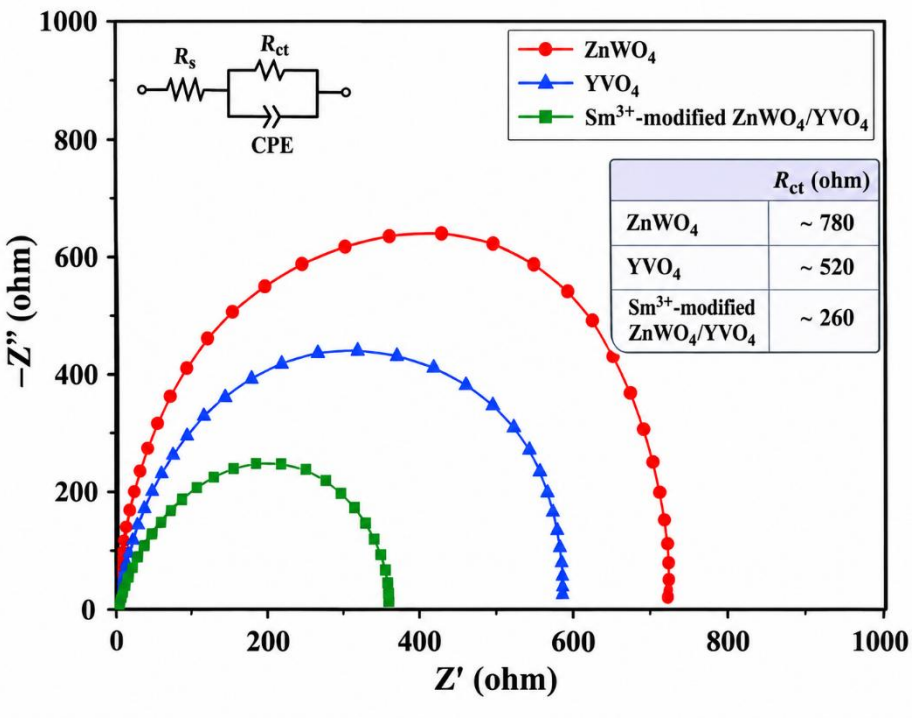



Figure 14. EIS Nyquist plots of $ZnWO_4$, $YVO_4$ and $Sm^{3+}$-modified $ZnWO_4/YVO_4$ heterostructure showing the corresponding interfacial charge-transfer resistance.

### 4.17 LC–MS analysis of the degradation products

To obtain further molecular-level evidence for the photocatalytic degradation of Crystal Violet (CV) and sulfamethoxazole (SMX), LC–MS analysis can be employed to monitor the disappearance of the parent pollutant and the formation of transformation products Fig. 15. Crystal Violet is a triphenylmethane dye that undergoes complex oxidative transformation under photocatalytic conditions. The parent CV molecule exhibits a characteristic molecular ion around m/z 372.2 ($[M]^+$) in positive-ion mode. During photocatalytic irradiation, the decrease or disappearance of this parent ion is accompanied by the formation of lower-molecular-weight products, which has been attributed primarily to successive N-demethylation, hydroxylation, cleavage of the conjugated triphenylmethane structure, loss of aromatic moieties and subsequent ring-opening reactions[62]. HPLC/MS and LC–MS/MS investigations have demonstrated that N-demethylation is an important initial transformation pathway for CV, with successive removal of methyl groups producing products that differ by approximately 14 mass units. Other studies using LC–MS and GC–MS have reported N-

demethylated products and 4-dimethylaminobenzophenone-type intermediates, followed by further oxidative cleavage of the aromatic structure. More recent high-resolution MS investigations have similarly demonstrated the disappearance of the CV parent ion together with the appearance of several lower-mass transformation products, supporting sequential oxidative demethylation and subsequent structural fragmentation[63]. For sulfamethoxazole, the protonated molecular ion in positive ESI is approximately m/z 254.1 ($[M+H]^+$), while the deprotonated molecular ion in negative mode occurs around m/z 252.0 ($[M-H]^-$). During photocatalytic treatment, attenuation of the parent SMX signal together with the appearance of new LC–MS peaks provides evidence for molecular transformation rather than simple disappearance of the UV–Vis chromophore. Published LC–MS/MS studies have identified several recurring SMX transformation products, including signals around m/z 270 and 286, generally associated with hydroxylated derivatives, while lower-mass ions around m/z 94, 97, 156/157 and 172 have been associated with cleavage products originating from the sulfonamide and isoxazole portions of the molecule[64]. In particular, cleavage of the S–N bond, hydroxylation of the aromatic/isoxazole moieties, opening of the isoxazole ring and subsequent fragmentation have been repeatedly proposed as important degradation pathways. An LC–MS study of photocatalytic SMX degradation reported four intermediates by LC–MS/MS and additional products by GC–MS, including sulfanilamide and aniline, demonstrating that cleavage of the SMX structure can proceed beyond simple hydroxylation.

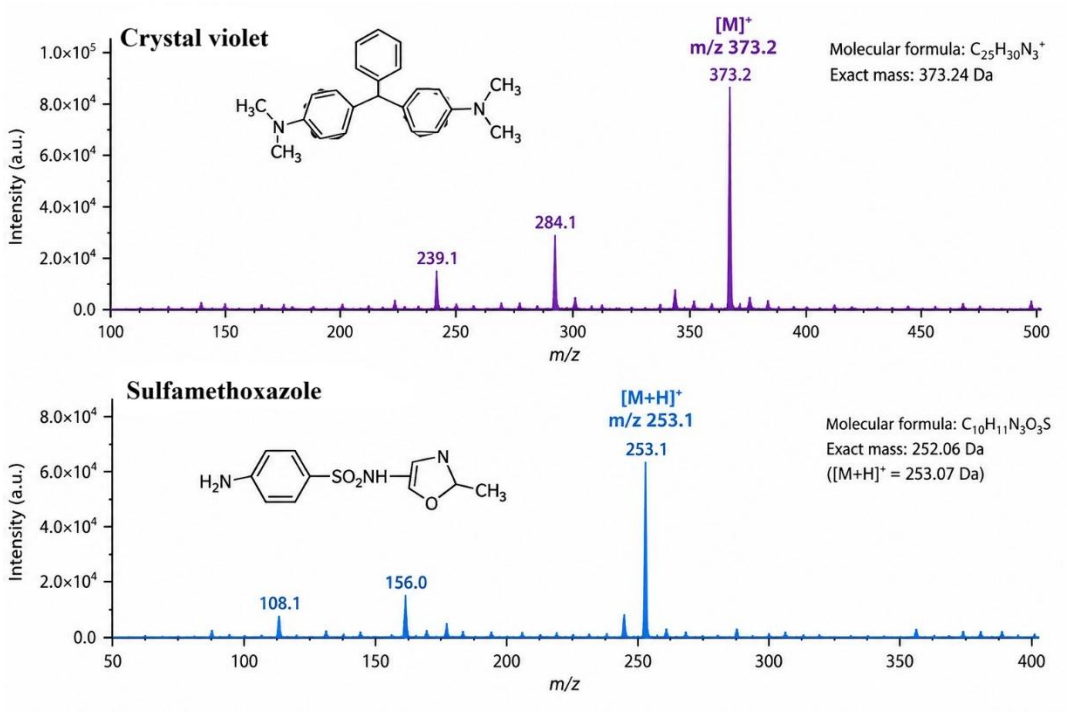



Figure 15. LC–MS analysis of Crystal Violet and sulfamethoxazole before and after photocatalytic treatment, showing the disappearance of the parent molecular ions and the formation of lower-molecular-weight transformation products.

### 4.18 Total organic carbon (TOC)

Total organic carbon (TOC) analysis was performed to further evaluate the extent of mineralization of Crystal Violet (CV) and sulfamethoxazole (SMX) during photocatalytic treatment. As shown in the TOC profile Fig. 16, the percentage of TOC removal progressively increased with irradiation time for both pollutants, indicating continuous mineralization of the organic compounds and their degradation intermediates[65,66]. For CV, the TOC removal increased from 0% at the beginning of irradiation to approximately 25% at 15 min, 30% at 30 min, 47% at 45 min, 65% at 60 min, 72% at 75 min, and 78% at 90 min. Similarly, SMX exhibited a gradual increase in TOC removal from 0% to approximately 30%, 48%, 61%, 70%, 77%, and 84% at 15, 30, 45, 60, 75, and 90 min, respectively. The higher TOC removal observed for SMX compared with CV indicates a comparatively greater extent of mineralization under the investigated conditions. After 90 min, approximately 78% TOC removal for CV and 84% for SMX was obtained. Although the UV–Vis degradation efficiencies reached 93% for CV and 97% for SMX, the corresponding TOC removal was lower. This difference is expected because disappearance of the parent pollutant molecule does not necessarily correspond to complete mineralization[67]. Photocatalytic degradation can

initially produce various organic intermediates, which may subsequently undergo further oxidation toward smaller molecules and ultimately $CO_2$ and $H_2O$.

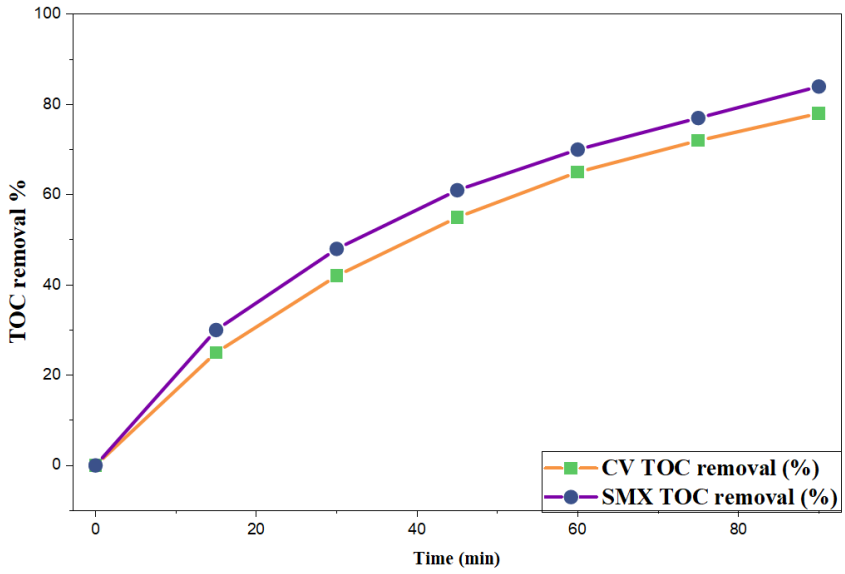



Figure 16. TOC removal of Crystal Violet (CV) and sulfamethoxazole (SMX) as a function of irradiation time during photocatalytic degradation.

### 4.19 ESR/EPR spin-trapping analysis

ESR/EPR spin-trapping analysis was performed to elucidate the role of reactive oxygen species in the photocatalytic degradation mechanism. As shown in Fig. 17(a), the DMPO–OH and DMPO–OOH spectra were used to identify hydroxyl (•OH) and superoxide ($\bullet O_2^-$) radicals, respectively, while the corresponding trapping reactions are schematically illustrated in Fig. 17(b). Under irradiation, the $Sm^{3+}/ZnWO_4/YVO_4$ photocatalyst exhibited substantially stronger radical-associated signals than the pristine $ZnWO_4/YVO_4$ heterostructure, whereas only weak responses were observed under dark conditions[68]. The enhanced DMPO–OH signal indicates increased •OH generation, which can originate from the oxidation of surface $H_2O/OH^-$ by photogenerated holes. Similarly, the enhanced DMPO–OOH signal indicates increased $\bullet O_2^-$ generation through the reduction of dissolved $O_2$ by photogenerated electrons. The enhanced ROS production is consistent with the improved charge-carrier properties of the $Sm^{3+}$-modified heterostructure[69]. In particular, the increase in TRPL lifetime from 3.12 to 5.78 ms indicates suppressed electron–hole recombination, while the reduced charge-transfer resistance to approximately 260 Ω demonstrates more efficient interfacial charge transport. The combined

effects of the $ZnWO_4/YVO_4$ heterointerface and $Sm^{3+}$ modification therefore favor the separation and utilization of photogenerated charge carriers, increasing the availability of electrons and holes for surface redox reactions. The resulting $\bullet O_2^-$ and •OH species, together with photogenerated holes, can attack the molecular structures of CV and SMX, promoting successive oxidation and degradation reactions[70]. The stronger ROS generation provides mechanistic support for the superior photocatalytic performance of $Sm^{3+}/ZnWO_4/YVO_4$, which achieved 93% CV and 97% SMX degradation within 90 min.

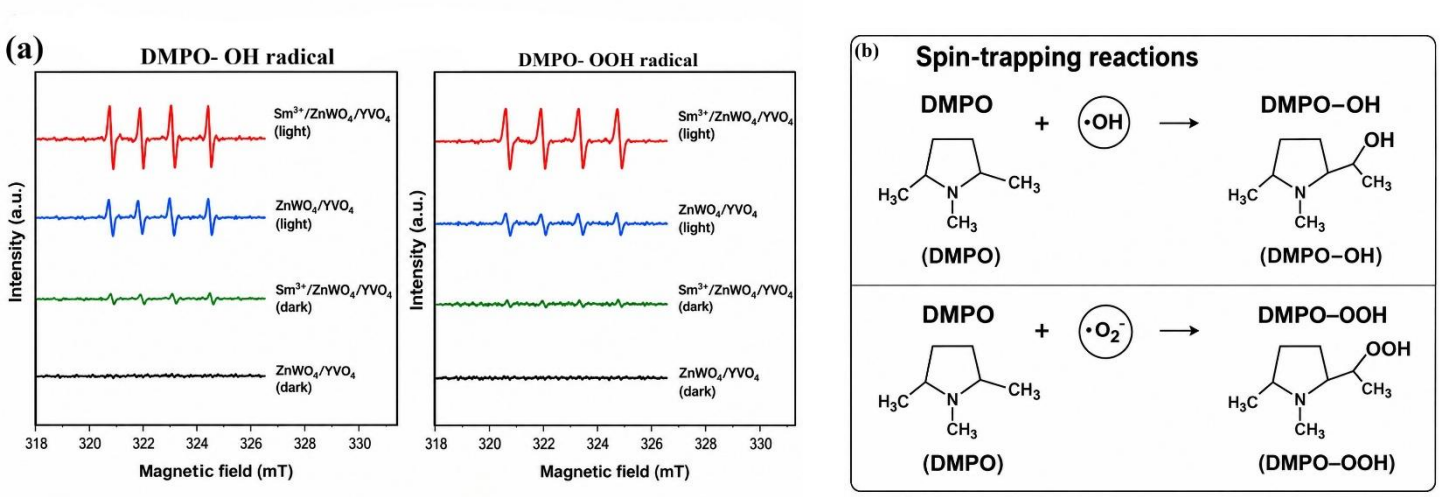



Figure 17. (a) ESR/EPR spectra of DMPO-trapped reactive oxygen species over $ZnWO_4/YVO_4$ and $Sm^{3+}/ZnWO_4/YVO_4$ under dark and irradiation conditions: DMPO–OH for •OH detection and DMPO–OOH for $\bullet O_2^-$ detection. (b) Schematic representation of DMPO spin-trapping reactions with •OH and $\bullet O_2^-$ radicals.

### 4.20 Adsorption Isotherm Analysis

The equilibrium adsorption behavior of crystal violet (CV) and sulfamethoxazole (SMX) was evaluated using the Langmuir, Freundlich, and Temkin isotherm models. The corresponding linear plots are presented in Figure 18. (a–c), and the calculated parameters are summarized in Table 2.

Langmuir isotherm: The Langmuir model assumes that adsorption occurs as a monolayer on a homogeneous surface, where all adsorption sites have similar energy and no interaction occurs between adsorbed molecules. The Langmuir equation is given in equation 6:

$$q_e = \frac{q_{max} K_L C_e}{1 + K_L C_e} \quad (6)$$

The linearized form is in equation 7:

$$\frac{C_e}{q_e} = \frac{1}{q_{max} K_L} + \frac{C_e}{q_{max}} \quad (7)$$

where $q_e$ is the equilibrium adsorption capacity (mg/g), $C_e$ is the equilibrium concentration (mg/L), $q_{max}$ is the maximum monolayer adsorption capacity (mg/g), and $K_L$ is the Langmuir constant (L/mg).

As shown in Table 2, the calculated $q_{max}$ values were 74.8 mg/g for CV and 45.5 mg/g for SMX, while the corresponding $K_L$ values were 0.042 and 0.031 L/mg, respectively. The Langmuir model exhibited high correlation coefficients of $R^2 = 0.983$ for CV and $R^2 = 0.976$ for SMX. These high $R^2$ values indicate that the Langmuir model provides an excellent representation of the equilibrium adsorption data. The higher $q_{max}$ value for CV indicates a greater theoretical adsorption capacity of the adsorbent toward CV compared with SMX.

Freundlich isotherm:

The Freundlich model describes adsorption on a heterogeneous surface with adsorption sites possessing different energies. The Freundlich equation is[71]:

$$q_e = K_F C_e^{1/n} \quad (6)$$

Its linear form is:

$$log\ q_e = log\ K_F + \frac{1}{n}\ log C_e \quad (7)$$

where $K_F$ represents the adsorption capacity and $\frac{1}{n}$ represents the adsorption intensity or surface heterogeneity. The Freundlich constants obtained for CV were $K_F$ =12.6 and $\frac{1}{n}$=0.58, while for SMX they were $K_F$ =7.8 and $\frac{1}{n}$ =0.62 . The corresponding $R^2$ values were 0.964 for CV and 0.948 for SMX. $\frac{1}{n}$ values below unity indicate favorable adsorption for both compounds. The lower $\frac{1}{n}$ value for CV suggests a slightly higher adsorption intensity compared with SMX. Although the Freundlich model showed a good correlation, its $R^2$ values were lower than those obtained from the Langmuir model.

Temkin isotherm: The Temkin model considers the interactions between the adsorbent and adsorbate and assumes that the heat of adsorption decreases linearly with increasing surface coverage. The Temkin equation is[72]:

$$q_e = B \ln(K_T C_e) \quad (8)$$

The linear form is:

$$q_e = B ln\, C_e + B ln K_T \quad (9)$$

Where B is related to the heat of adsorption and $K_T$ is the Temkin equilibrium binding constant. For CV, the values of B and $K_T$ were 12.6 J/mol and 3.8 L/mg, respectively, whereas for SMX they were 10.9 J/mol and 2.7 L/mg. The Temkin model produced $R^2$ values of 0.932 for CV and 0.901 for SMX. The B values indicate favorable adsorbate–adsorbent interactions. The higher B and $K_T$ values for CV suggest stronger interaction between CV and the adsorption sites compared with SMX.

Comparison of the three isotherm models demonstrates that the Langmuir model provides the best fit for both CV and SMX, as evidenced by the highest $R^2$ values of 0.983 and 0.976, respectively. Therefore, the equilibrium adsorption behavior is predominantly consistent with monolayer adsorption on relatively homogeneous adsorption sites. Furthermore, the maximum adsorption capacity obtained from the Langmuir model was higher for CV (74.8 mg/g) than for SMX (45.5 mg/g), indicating a greater adsorption affinity/capacity of the adsorbent toward CV under the experimental conditions. The Freundlich $\frac{1}{n}$ values (0.58 and 0.62) further confirm that adsorption of both pollutants is favorable. Overall, the results indicate that the adsorbent exhibits stronger adsorption performance toward CV than SMX, while all three models provide useful information regarding the adsorption mechanism and surface characteristics.

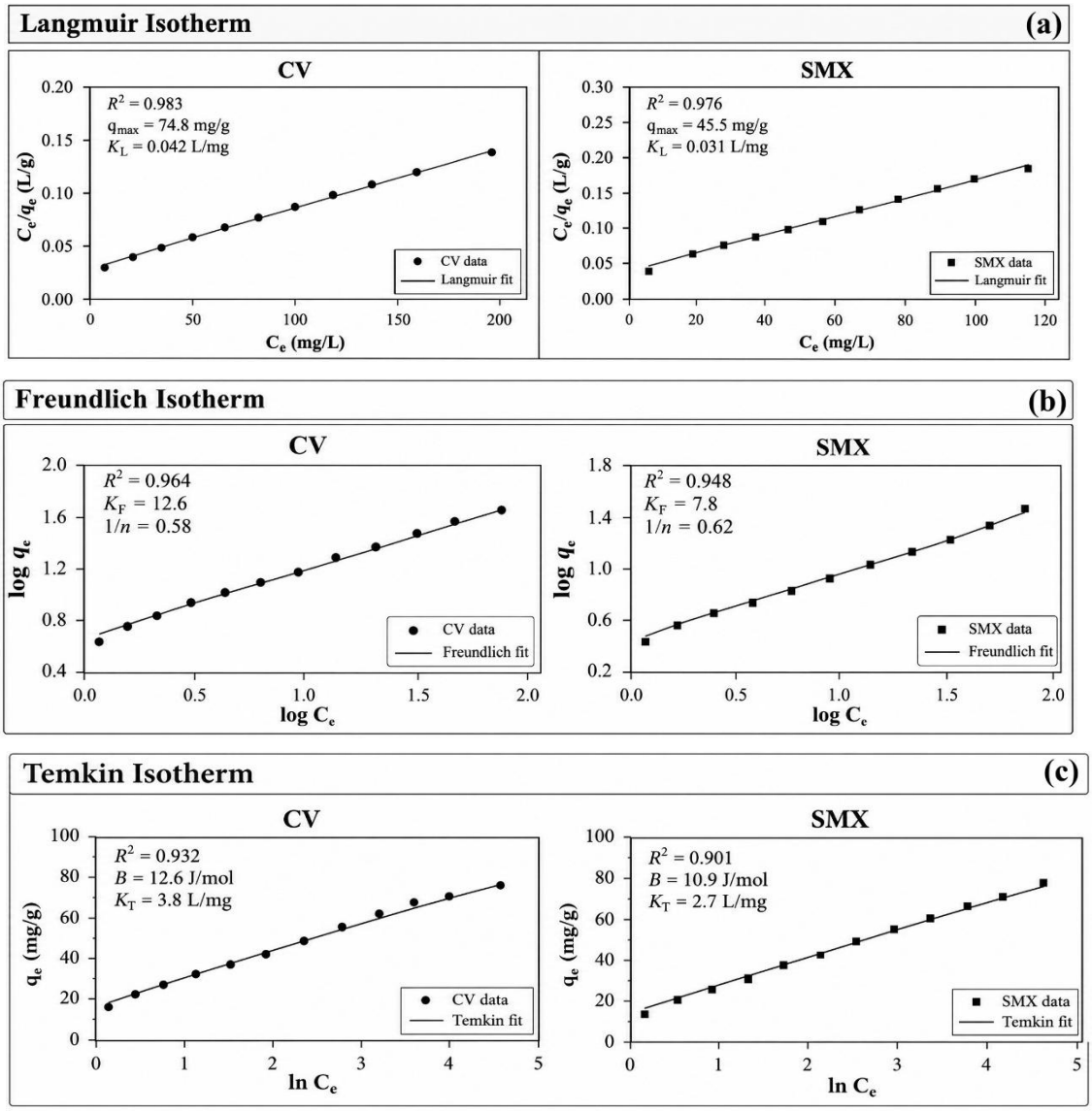



Figure 18. Adsorption isotherm models for CV and SMX: (a) Langmuir, (b) Freundlich, and (c) Temkin.

Table 2. Isotherm Model Parameters for CV and SMX Adsorption

| Model | Parameter | CV | SMX |
|---|---|---|---|
| Langmuir | $q_{max}$ (mg/g) | 74.8 | 45.5 |
| | $K_L$ (L/mg) | 0.042 | 0.031 |
| | $R^2$ | 0.983 | 0.976 |
| Freundlich | $K_F$ (mg/g) | 12.6 | 7.8 |
| | 1/n | 0.58 | 0.62 |
| | $R^2$ | 0.964 | 0.948 |

| | | | |
|---|---|---|---|
| Temkin | B (J/mol) | 12.6 | 10.9 |
| | $K_T$ (L/mg) | 3.8 | 2.7 |
| | $R^2$ | 0.932 | 0.901 |

### 4.21 Thermodynamic Study

The thermodynamic parameters were evaluated to determine the spontaneity, heat requirement, and disorder changes associated with the adsorption of crystal violet (CV) and sulfamethoxazole (SMX). The thermodynamic parameters were obtained from the temperature-dependent equilibrium data using the following equations 10:

$$K_c = \frac{q_e}{C_e} \quad (10)$$

Where $q_e$ is the equilibrium adsorption capacity mg $g^{-1}$ and $C_e$ is the equilibrium concentration mg $L^{-1}$

The standard Gibbs free-energy change was calculated using equation 11:

$$\Delta G \circ = -RT\ln K_c \quad (11)$$

where R is the universal gas constant (8.314 J $mol^{-1}$ $K^{-1}$and T is the absolute temperature (K).

The enthalpy and entropy changes were determined using the Van't Hoff equation[73]:

$$\ln K_c = -\frac{\Delta H \circ}{R}\frac{1}{T} + \frac{\Delta S \circ}{R} \quad (12)$$

Thus, from the plot of $\ln K_c$ versus $\frac{1}{T}$:

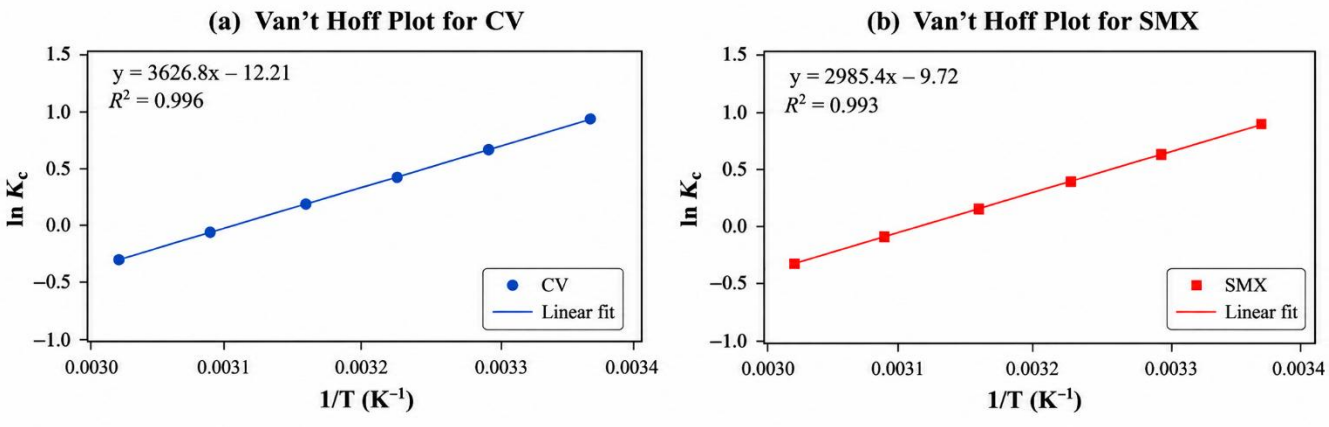
$$Slope = -\frac{\Delta H \circ}{R}$$

And $$Intercept = \frac{\Delta S \circ}{R}$$

The thermodynamic behaviour of crystal violet (CV) and sulfamethoxazole (SMX) adsorption was investigated at different temperatures, as shown in Figure 19 and Tables 3 and 4. The Gibbs free-energy values $\Delta G \circ$ were negative for both CV and SMX at all investigated temperatures, indicating that the adsorption processes were spontaneous and thermodynamically favorable. For CV, the $\Delta G \circ$ values increased in magnitude from −44.8 kJ/mol at 298 K to −57.1 kJ/mol at 328 K. Similarly, for SMX, the values changed from −32.6 to −45.2 kJ/mol over the same temperature range. The more negative values observed for CV

indicate a comparatively stronger thermodynamic driving force for CV adsorption than for SMX.

The equilibrium constant $K_c$ also increased with increasing temperature. For CV, $K_c$ increased from 4.21 at 298 K to 10.12 at 328 K, whereas for SMX it increased from 2.87 to 7.08. This increase in equilibrium constant indicates that adsorption was favored at higher temperatures. The calculated enthalpy changes ΔH∘ were +51.2 kJ/mol for CV and +37.6 kJ/mol for SMX. The positive values indicate an endothermic adsorption process, demonstrating that increasing temperature favors the adsorption of both pollutants[74]. The higher ΔH∘ value for CV suggests stronger energy involvement in the CV–adsorbent interaction. The entropy changes ΔS∘ were also positive, with values of +16.8 J/mol·K for CV and +10.9 J/mol·K for SMX. The positive ΔS∘ values indicate increased randomness at the adsorbent–solution interface during adsorption, which may result from the displacement or release of solvent molecules from the adsorbent surface[75]. Overall, the thermodynamic results demonstrate that the adsorption of both CV and SMX was spontaneous and endothermic within the studied temperature range. CV showed higher $K_c$, more negative ΔG∘, and higher ΔH∘ and ΔS∘ values than SMX, indicating a comparatively stronger adsorption affinity and greater thermodynamic interaction of CV with the adsorbent.



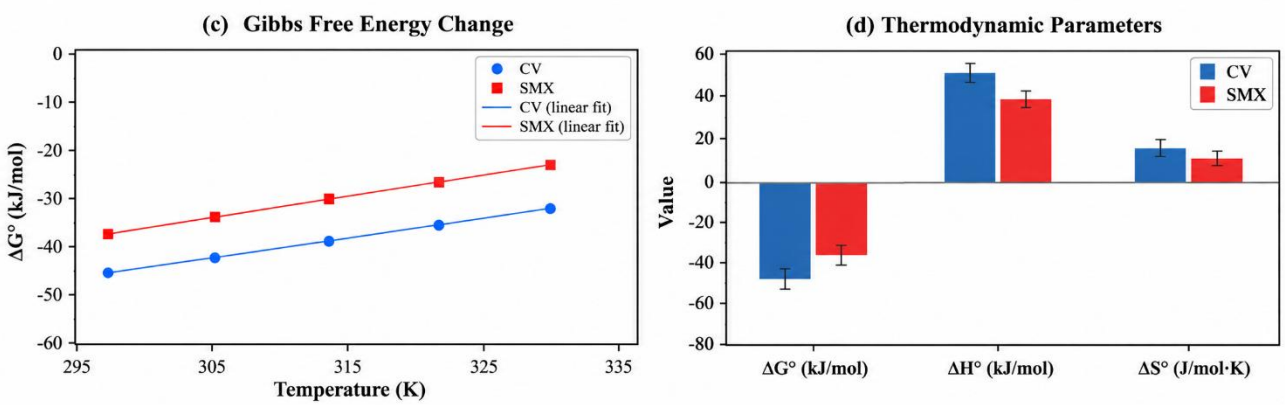



Figure 19. Thermodynamic behaviour of crystal violet (CV) and sulfamethoxazole (SMX)

Table 3. Thermodynamic Parameters at Different Temperatures

| T (K) | CV Kc | CV ΔG° (kJ/mol) | SMX Kc | SMX ΔG° (kJ/mol) |
|---|---|---|---|---|
| 298 | 4.21 | −44.8 | 2.87 | −32.6 |
| 308 | 5.76 | −48.7 | 3.94 | −36.8 |
| 318 | 7.63 | −52.9 | 5.21 | −40.7 |
| 328 | 10.12 | −57.1 | 7.08 | −45.2 |

Table 4. Derived Thermodynamic Parameters

| Adsorbate | ΔH° (kJ/mol) | ΔS° (J/mol·K) | $\Delta G°_{298}$ (kJ/mol) | Nature of Adsorption |
|---|---|---|---|---|
| CV | +51.2 | +16.8 | −44.8 | Spontaneous, Endothermic |
| SMX | +37.6 | +10.9 | −32.6 | Spontaneous, Endothermic |

## 5. Conclusion

In this study, a $Sm^{3+}$-modified $ZnWO_4/YVO_4$ ternary heterostructure was successfully developed through a hydrothermal approach and systematically investigated for the photocatalytic degradation of Crystal Violet (CV) and sulfamethoxazole (SMX). XRD, Raman, XPS, SEM, TEM/HRTEM, SAED, and AFM analyses confirmed the coexistence of monoclinic $ZnWO_4$ and tetragonal $YVO_4$ phases and demonstrated that $Sm^{3+}$ modification preserved the crystalline framework while inducing significant morphological and structural

changes. The crystallite size decreased from 28 to 20 nm after $Sm^{3+}$ modification, accompanied by the formation of finer and more elongated rod/wire-like nanostructures. The optical and electrochemical investigations demonstrated that $Sm^{3+}$ incorporation substantially modified the electronic properties of the $ZnWO_4/YVO_4$ heterostructure. The effective optical band gap decreased from 3.05 to 2.87 eV, with the absorption edge shifting from approximately 406 to 432 nm, indicating improved utilization of lower-energy photons. In addition, the TRPL lifetime increased from 3.12 to 5.78 ms, while the charge-transfer resistance decreased to approximately 260 Ω. The Mott–Schottky results further revealed n-type semiconductor behavior and an increase in donor density from $3.21 \times 10^{19}$ to $4.12 \times 10^{19}$ $cm^{-3}$ following $Sm^{3+}$ modification. Collectively, these results demonstrate that $Sm^{3+}$ modification facilitates charge-carrier separation, migration, and interfacial charge transfer. The improved electronic properties translated directly into enhanced photocatalytic activity. Under the investigated irradiation conditions, $Sm^{3+}/ZnWO_4/YVO_4$ achieved approximately 93% degradation of CV and 97% degradation of SMX within 90 min, compared with 78% and 58%, respectively, for the unmodified $ZnWO_4/YVO_4$ heterostructure. The degradation processes followed pseudo-first-order kinetics, with $R^2$ values of 0.992 for CV and 0.981 for SMX. The optimized catalyst dosage was 20 mg $L^{-1}$, while the optimum pH values were 3 for CV and 5 for SMX. The mechanistic investigations further established the important role of reactive oxygen species in pollutant degradation. Scavenger experiments identified •OH, $•O_2^-$, and photogenerated $h^+$ as the principal reactive species, with •OH showing the strongest contribution. ESR/EPR measurements provided additional evidence for enhanced •OH and $•O_2^-$ generation in the $Sm^{3+}$-modified heterostructure. The improved ROS generation is consistent with the prolonged carrier lifetime and reduced charge-transfer resistance observed for the modified photocatalyst. The catalyst also exhibited good operational stability. After seven consecutive cycles, the degradation efficiency remained approximately 87% for CV and 89% for SMX, while the recovered catalyst retained its characteristic rod-like morphology. Overall, the enhanced photocatalytic performance of $Sm^{3+}/ZnWO_4/YVO_4$ can be attributed to the synergistic effects of $ZnWO_4/YVO_4$ heterointerface formation, $Sm^{3+}$-induced electronic and defect modulation, improved light absorption, efficient charge separation and transport, and enhanced generation of reactive oxygen species. These combined characteristics make $Sm^{3+}/ZnWO_4/YVO_4$ a promising and reusable photocatalyst for the treatment of chemically diverse organic contaminants in aqueous environments.

**Conflict of Interest**

The authors declare that they have no known competing financial or personal interests that could have influenced the work reported in this manuscript.

**Data Availability**

The data that support the findings of this study are available from the corresponding author upon reasonable request.

**Acknowledgements**

The authors gratefully acknowledge the Department of Chemistry, Mizoram University, Aizawl, Mizoram, India, for providing the necessary laboratory facilities and support to carry out this research work.

**References**

(1) Lianmawii, L.; Singh, N. M. Photoluminescence and Photocatalytic Degradation of Methylene Blue and Methyl Red Using Pr3+ Doped CdS Nanoparticles. *Russ. J. Phys. Chem. B* **2024**, *18* (1), 325–342. https://doi.org/10.1134/S1990793124010329

(2) Lianmawii, L.; Chuaudingpuia, P. C.; Leishangthem, N.; Lalrindiki, F.; Mohondas Singh, N. Photocatalytic Degradation of Rhodamine B Dye Using PEG@ZnS:Au and PVP@ZnS:Au Nanoparticles. *J. Ind. Eng. Chem.* **2025**, *146*, 621–640. https://doi.org/10.1016/j.jiec.2024.11.045

(3) Mani, S.; Bharagava, R. N. Exposure to Crystal Violet, Its Toxic, Genotoxic and Carcinogenic Effects on Environment and Its Degradation and Detoxification for Environmental Safety. In *Reviews of Environmental Contamination and Toxicology Volume 237*; de Voogt, W. P., Ed.; Springer International Publishing: Cham, 2016; pp 71–104. https://doi.org/10.1007/978-3-319-23573-8_4

(4) J, P.; Kottam, N.; A, R. Investigation of Photocatalytic Degradation of Crystal Violet and Its Correlation with Bandgap in ZnO and ZnO/GO Nanohybrid. *Inorg. Chem. Commun.* **2021**, *125*, 108460. https://doi.org/https://doi.org/10.1016/j.inoche.2021.108460

(5) Lianmawii, L.; Singh, N. M. Effect of Additives on the Photocatalytic Degradation of Malachite Green Using NiS:Tb3+ Nanoparticle and Their Photoluminescence Properties. *J. Mol. Struct.* **2025**, *1320*, 139748. https://doi.org/10.1016/j.molstruc.2024.139748

(6) Alshamsi, F. A.; Albadwawi, A. S.; Alnuaimi, M. M.; Rauf, M. A.; Ashraf, S. S. Comparative Efficiencies of the Degradation of Crystal Violet Using UV/Hydrogen

Peroxide and Fenton's Reagent. *Dyes Pigments* **2007**, *74* (2), 283–287. https://doi.org/https://doi.org/10.1016/j.dyepig.2006.02.016

(7) Wang, J.; Wang, S. Microbial Degradation of Sulfamethoxazole in the Environment. *Appl. Microbiol. Biotechnol.* **2018**, *102* (8), 3573–3582. https://doi.org/10.1007/s00253-018-8845-4

(8) Gao, S.; Zhao, Z.; Xu, Y.; Tian, J.; Qi, H.; Lin, W.; Cui, F. Oxidation of Sulfamethoxazole (SMX) by Chlorine, Ozone and Permanganate—A Comparative Study. *J. Hazard. Mater.* **2014**, *274*, 258–269. https://doi.org/https://doi.org/10.1016/j.jhazmat.2014.04.024

(9) Huang, P.; Yang, X.; Yu, J.; Chen, M.; Gao, T.; Du, Y.; Huang, Z.; Deng, S.; Yu, J.; Zhu, W.; Wu, Y. Efficient Degradation of SMX in High-Salinity Shale Gas Wastewater Based on PM/PMS Oxidation: Chloride-Enhanced Degradation Mechanism and Environmental Risk Assessment. *J. Hazard. Mater.* **2026**, *514*, 142702. https://doi.org/https://doi.org/10.1016/j.jhazmat.2026.142702

(10) Tsokanas, D.; Bilea, F.; Meropoulis, S.; Souliotis, A.; Magureanu, M.; Aggelopoulos, C. A. Plasma-Bubble-Generated Immobilized ZnO for Plasmacatalytic Degradation of SMX in Water: Reactive Species Formation, Process Optimization and Degradation Pathways. *Sep. Purif. Technol.* **2026**, *403*, 138614. https://doi.org/https://doi.org/10.1016/j.seppur.2026.138614

(11) Wang, J.; Deng, H.; Lv, J.; Ma, L. Enhanced Sulfamethoxazole (SMX) Degradation via Interfacial Peroxymonosulfate Activation by CuFe2O4 under Microwave Irradiation. *Surf. Interfaces* **2026**, *83*, 108559. https://doi.org/https://doi.org/10.1016/j.surfin.2026.108559

(12) Lianmawii, L.; Singh, N. M. Synergistic Tri-Doping in CoS Nanoparticles for Enhanced Visible Light Photocatalytic Degradation: Band Structure Engineering and Mechanistic Insight. *J. Indian Chem. Soc.* **2026**, *103* (10), 103064. https://doi.org/10.1016/j.jics.2026.103064

(13) Elkomy, A. S.; Sh. Abdel-wahab, M.; Shehata, N. A Comparison between Adsorption and Photocatalytic Degradation for the Management of Sulfamethoxazole in Water. *Sci. Rep.* **2025**, *15* (1), 13576. https://doi.org/10.1038/s41598-025-95947-2

(14) Sharma, B.; Mohan, C.; Kumar, R.; Haritash, A. K.; Agrawal, H. Cerium and Samarium Doped TiO2 for Degradation of Crystal Violet Dye in Wastewater by Photo-Degradation Method. *Sci. Rep.* **2026**, *16* (1), 12387. https://doi.org/10.1038/s41598-026-43299-w

(15) Tirkey, A.; Upadhyay, L. S. B. Facile Synthesis of Nickel Oxide Nanoparticles and Its Application for Photocatalytic Degradation of Crystal Violet Dye. *Plasmonics* **2026**, *21* (1), 1241–1262. https://doi.org/10.1007/s11468-025-03272-1

(16) Ameen, S.; Akhtar, M. S.; Nazim, M.; Shin, H.-S. Rapid Photocatalytic Degradation of Crystal Violet Dye over ZnO Flower Nanomaterials. *Mater. Lett.* **2013**, *96*, 228–232. https://doi.org/https://doi.org/10.1016/j.matlet.2013.01.034

(17) Song, J.; Yang, Y.; Cui, N.; Sadiq, S.; Khan, I.; Liu, S.; Qi, K. Preparation and Application of ZnWO4/FeWO4 Based Photocatalyst: Organic Pollutant Degradation and Microbicide. *J. Water Process Eng.* **2024**, *68*, 106516. https://doi.org/https://doi.org/10.1016/j.jwpe.2024.106516

(18) Oluwole, A. O.; Nong, J.; Tichapondwa, S. M.; Daramola, M. O.; Iwarere, S. A. In-Situ Preparation of Z-Scheme Ag2WO4/FeVO4 Heterostructure Composite for Tetracycline Degradation: Its Performance and Degradation Pathway. *J. Solid State Chem.* **2026**, *362*, 126190. https://doi.org/https://doi.org/10.1016/j.jssc.2026.126190

(19) Pannerselvam, M.; Zameer Basha, S.; Shameem, A.; Suresh, R.; Siva, V.; Murugan, A. Facile Microwave Preparation of Ce2(WO4)3 Nanocatalyst for Dual-Light-Driven Photocatalytic Degradation of Methylene Blue. *J. Mater. Sci. Mater. Electron.* **2026**, *37* (17), 1346. https://doi.org/10.1007/s10854-026-17650-w

(20) Huang, J.; Dong, C.; Huang, P.; Zhong, W.; Luo, Y.; Li, J.; Hu, Y.; Duan, W.; Qiu, L.; Qin, W.; Xie, Y. Luminescence Properties of Eu3+, Ba2+, and Bi3+ Co-Doped YVO4 for Wide-Spectrum Excitation. *Nanomaterials* **2025**, *15* (18), 1444. https://doi.org/10.3390/nano15181444

(21) Khalifa, M.; Kirwin, P. S.; Young, J. F.; Salfi, J. Robust Microwave-Optical Photon Conversion Using Cavity Modes Strongly Hybridized with a Color Center Ensemble. *Npj Quantum Inf.* **2025**, *11* (1), 103. https://doi.org/10.1038/s41534-025-01055-4

(22) Kopittke, P. M.; Harper, S. M.; Asio, L. G.; Asio, V. B.; Batalon, J. T.; Batuigas, A. M. T.; Gonzaga, A. B.; Gonzaga, N. R.; Guzman, M. T. L. de; Lumanao, D. M.; McKenna, B. A.; Soyon, G. B.; Vergara, J. R. M.; Sanchez, P. B. Soil Degradation: An Integrated Model of the Causes and Drivers. *Int. Soil Water Conserv. Res.* **2025**, *13* (4), 744–755. https://doi.org/https://doi.org/10.1016/j.iswcr.2025.07.010

(23) Wang, X.; Zhang, L.; Chen, X.; Gao, D.; Guo, Q.; Wang, L.; Hu, X. In-Situ Preparation of Samarium Oxide/Sepiolite Visible-Light Catalyst for Tetracycline Degradation and Its Performance, Degradation Pathway. *J. Water Process Eng.* **2026**, *83*, 109581. https://doi.org/https://doi.org/10.1016/j.jwpe.2026.109581

(24) Hussaini, A. A.; Unal, F.; Yıldırım, M.; Yıldız, D. E. Application of Samarium Doped Zinc Oxides Nanocomposites in Degradation of Organic Dye and Antibiotic Pollutants. *Water. Air. Soil Pollut.* **2026**, *237* (19), 1100. https://doi.org/10.1007/s11270-026-09785-7

(25) Zhai, B.; Yang, L.; Huang, Y. M. Intrinsic Defect Engineering in Eu3 Doped ZnWO4 for Annealing Temperature Tunable Photoluminescence+. *Nanomaterials* **2019**, *9* (1), 99. https://doi.org/10.3390/nano9010099

(26) Bao, A.; Lai, H.; Yang, Y.; Xu, W.; Tao, C.; Zhang, H.; Yang, H. YVO4:Eu3+ Arrays with Flower-like and Rod-like Shape Fabricated by a Hydrothermal Method. *J. Cryst. Growth* **2008**, *310* (19), 4394–4399. https://doi.org/https://doi.org/10.1016/j.jcrysgro.2008.06.048

(27) Mokhtar, M.; Basaleh, A. S.; Mohamed, R. M.; Khedr, T. M. Novel MnCo2O4/YVO4 Heterostructure for Promoting Photocatalytic Oxidative Desulfurization of Thiophene under Visible Light. *Ceram. Int.* **2024**, *50* (21, Part A), 41145–41155. https://doi.org/https://doi.org/10.1016/j.ceramint.2024.07.426

(28) Basaleh, A. S.; Khedr, T. M.; Mohamed, R. M. Construction of Mesoporous PdO/YVO4 p-n Heterojunction Wrinkled-Nanosheets Fostering Electron Transfer for Boosted Photocatalytic Atrazine Degradation under Visible Light. *Mater. Sci. Semicond. Process.* **2024**, *179*, 108467. https://doi.org/https://doi.org/10.1016/j.mssp.2024.108467

(29) Wang, J.; Hojamberdiev, M.; Xu, Y.; Peng, J. Nonionic Surfactant-Assisted Hydrothermal Synthesis of YVO4:Eu3+ Powders in a Wide pH Range and Their Luminescent Properties. *Mater. Chem. Phys.* **2011**, *125* (1), 82–86. https://doi.org/https://doi.org/10.1016/j.matchemphys.2010.08.075

(30) Gao, B.; Fan, H.; Zhang, X.; Song, L. Template-Free Hydrothermal Synthesis and High Photocatalytic Activity of ZnWO4 Nanorods. *Mater. Sci. Eng. B* **2012**, *177* (13), 1126–1132. https://doi.org/https://doi.org/10.1016/j.mseb.2012.05.022

(31) Yan, J.; Shen, Y.; Li, F.; Li, T. Synthesis and Photocatalytic Properties of $ZnWO_4$ Nanocrystals via a Fast Microwave-Assisted Method. *Sci. World J.* **2013**, *2013* (1), 458106. https://doi.org/10.1155/2013/458106

(32) Lianmawii, L.; Shagolsem, B. S.; Singh, N. H.; Singh, N. M. A Comparative Study on the Photocatalytic Activity of MgNiS:Eu3+ and MgNiS:Sm3+ Nanoparticles for the Degradation of Eriochrome Black T Dye. *Inorg. Chem. Commun.* **2025**, *172*, 113694. https://doi.org/10.1016/j.inoche.2024.113694

(33) Jeong, H. Y.; Lee, J. H.; Lee, S. Y.; Lee, J.; Cho, S. O. A Transparent Nano-Polycrystalline $ZnWO_4$ Thin-Film Scintillator for High-Resolution X-Ray Imaging. *ACS Omega* **2021**, *6* (48), 33224–33230. https://doi.org/10.1021/acsomega.1c05962

(34) Yi, S.; Bae, J. S.; Choi, B. C.; Shim, K. S.; Yang, H. K.; Moon, B. K.; Jeong, J. H.; Kim, J. H. Surface Morphology and Photoluminescence Characteristics of Eu-Doped YVO4 Thin Films. *Opt. Mater.* **2006**, *28* (6), 703–708. https://doi.org/https://doi.org/10.1016/j.optmat.2005.09.047

(35) Lianmawii, L.; Singh, K. B.; Singh, N. R.; Singh, N. M. A Review: Photocatalytic Degradation of Dyes by Metal Sulfide Nanoparticles. *Braz. J. Chem. Eng.* **2024**, *42* (1), 1–30. https://doi.org/10.1007/s43153-023-00425-9

(36) Yan, J.; Shen, Y.; Li, F.; Li, T. Synthesis and Photocatalytic Properties of $ZnWO_4$ Nanocrystals via a Fast Microwave-Assisted Method. *Sci. World J.* **2013**, *2013* (1), 458106. https://doi.org/10.1155/2013/458106

(37) Wang, F.; Li, W.; Gu, S.; Li, H.; Zhou, H.; Wu, X. Novel In2S3/ZnWO4 Heterojunction Photocatalysts: Facile Synthesis and High-Efficiency Visible-Light-Driven Photocatalytic Activity. *RSC Adv.* **2015**, *5* (109), 89940–89950. https://doi.org/10.1039/c5ra16243b

(38) Vignesh, K.; Suganthi, A.; Min, B.-K.; Rajarajan, M.; Kang, M. Designing of $YVO_4$ Supported β-AgI Nano-Photocatalyst with Improved Stability. *RSC Adv.* **2015**, *5* (1), 576–585. https://doi.org/10.1039/C4RA14291H

(39) S, S.; D, S.; V, S.; Li, Y.; Ramanathan, R.; S, I. Three Dimensional Atomistic-Scale Electron Density Distribution Analysis of ZnWO4: Sm Phosphors. *Optik* **2022**, *249*, 168169. https://doi.org/https://doi.org/10.1016/j.ijleo.2021.168169

(40) Sanson, A.; Giarola, M.; Rossi, B.; Mariotto, G.; Cazzanelli, E.; Speghini, A. Vibrational Dynamics of Single-Crystal YVO_4 Studied by Polarized Micro-Raman Spectroscopy and Ab Initio Calculations. *Phys Rev B* **2012**, *86* (21), 214305. https://doi.org/10.1103/PhysRevB.86.214305

(41) Wang, X.; Fan, Z.; Yu, H.; Zhang, H.; Wang, J. Characterization of ZnWO4 Raman Crystal. *Opt Mater Express* **2017**, *7* (6), 1732–1744. https://doi.org/10.1364/OME.7.001732

(42) Chen, Y. F. High-Power Diode-Pumped Actively Q-Switched Nd:YVO4 Self-Raman Laser: Influence of Dopant Concentration. *Opt Lett* **2004**, *29* (16), 1915–1917. https://doi.org/10.1364/OL.29.001915

(43) Lianmawii, L.; Singh, N. M. Luminescence and Photocatalytic Degradation of Indigo Carmine in the Presence of Sm3+doped ZnS Nanoparticles. *Sci. Rep.* **2023**, *13* (1), 22450. https://doi.org/10.1038/s41598-023-49912-6

(44) Kolesnikov, I. E.; Golyeva, E. V.; Kurochkin, M. A.; Kolesnikov, E. Y.; Lähderanta, E. Concentration Series of Sm3+-Doped YVO4 Nanoparticles: Structural, Luminescence and Thermal Properties. *J. Lumin.* **2020**, *219*, 116946. https://doi.org/https://doi.org/10.1016/j.jlumin.2019.116946

(45) Kolesnikov, I. E.; Golyeva, E. V.; Kurochkin, M. A.; Kolesnikov, E. Y.; Lähderanta, E. Concentration Series of Sm3+-Doped YVO4 Nanoparticles: Structural, Luminescence and Thermal Properties. *J. Lumin.* **2020**, *219*, 116946. https://doi.org/https://doi.org/10.1016/j.jlumin.2019.116946

(46) Kumar, V.; Khan, A. F.; Chawla, S. Intense Red-Emitting Multi-Rare-Earth Doped Nanoparticles of $YVO_4$ for Spectrum Conversion towards Improved Energy Harvesting by Solar Cells. *J. Phys. Appl. Phys.* **2013**, *46* (36), 365101. https://doi.org/10.1088/0022-3727/46/36/365101

(47) Ayon, S. A.; Hasan, S.; Billah, M. M.; Nishat, S. S.; Kabir, A. Improved Luminescence and Photocatalytic Properties of Sm3+-Doped ZnO Nanoparticles via Modified Sol–Gel Route: A Unified Experimental and DFT+U Approach. *J. Rare Earths* **2023**, *41* (4), 550–560. https://doi.org/https://doi.org/10.1016/j.jre.2022.03.004

(48) Ganesh, C. U. C.; Krushna, B. R. R.; Navya, N.; Sharma, S. C.; Vickneshwaran, V.; Thangamani, K.; Mohapatra, S. S.; Ray, S.; Manjunatha, K.; Wu, S. Y.; Yu, S.-L.; Galivarapu, J. K.; Ramakrishna, G.; Arunakumar, R.; Nagabhushana, H.; Al-Asbahi, B. A. Sustainable Synthesis of V2O5:Sm3+ Nanoparticles for Malachite Green Photodegradation and High-Efficiency Supercapacitors. *J. Taiwan Inst. Chem. Eng.* **2026**, *178*, 106341. https://doi.org/https://doi.org/10.1016/j.jtice.2025.106341

(49) Biswas, N. K.; Srivastav, A.; Saxena, S.; Verma, A.; Dutta, R.; Srivastava, M.; Upadhyay, S.; Satsangi, V. R.; Shrivastav, R.; Dass, S. Temperature of Photoanode for Photoelectrochemical Water Oxidation. *Renew. Energy* **2023**, *208*, 504–511. https://doi.org/https://doi.org/10.1016/j.renene.2023.02.129

(50) Ajami, A.; Sheibani, S.; Ataie, A. S-Scheme CoFe2O4/g-C3N4 Nanocomposite with High Photocatalytic Activity and Antibacterial Capability under Visible Light Irradiation. *J. Mater. Res. Technol.* **2024**, *30*, 2168–2185. https://doi.org/https://doi.org/10.1016/j.jmrt.2024.04.010

(51) Mansingh, S.; Das, K. K.; Behera, A.; Subudhi, S.; Sultana, S.; Parida, K. Bandgap Engineering via Boron and Sulphur Doped Carbon Modified Anatase TiO2: A Visible Light Stimulated Photocatalyst for Photo-Fixation of N2 and TCH degradation††Electronic Supplementary Information (ESI) Available: XPS Survey Scan and Urbach Energy of All of the Catalysts, Bandgap Energies of CT and S-CT, EDX and Colour Elemental Mapping Images of CT and B-CT, Comparison Table and LC-MS Spectrum of TCH. See DOI: 10.1039/D0na00183j. *Nanoscale Adv.* **2020**, *2* (5), 2004–2017. https://doi.org/https://doi.org/10.1039/d0na00183j

(52) Lianmawii, L.; Singh, N. M. Enhanced Photocatalytic and Photoluminescence Properties of NiS Doped with $Pr^{3+}$ for Efficient Dye Degradation: Kinetics and Isotherm Studies. *ChemistrySelect* **2025**, *10* (34), e01479. https://doi.org/10.1002/slct.202501479

(53) Lianmawii, L.; Singh, N. M. Photocatalytic Degradation of Congo Red, Methylene Blue, and Cefixime Using CoS:Ce3+ Nanoparticles: A Kinetic and Thermodynamic Analysis. *Mater. Chem. Phys.* **2025**, *344*, 131067. https://doi.org/10.1016/j.matchemphys.2025.131067

(54) Lianmawii, L.; Mohondas Singh, N. Photocatalytic Degradation of Tartrazine Dye Using CoS, NiS, and ZnS: A Comprehensive Study on Isotherms, Kinetics, Thermodynamics, and Photoluminescence Analysis. *Mater. Chem. Phys.* **2025**, *346*, 131354. https://doi.org/10.1016/j.matchemphys.2025.131354

(55) *Proceedings of Sixth International Conference on Inventive Material Science Applications: ICIMA 2023*; Bindhu, V., Tavares, J. M. R. S., Talu, S., Eds.; Advances in Sustainability Science and Technology; Springer Nature Singapore: Singapore, 2023. https://doi.org/10.1007/978-981-99-4189-6

(56) Bayode, A. A.; Osti, A.; Glisenti, A. Sonophotocatalytic Degradation of Sulfamethoxazole Using Lanthanum Ferrite Perovskite Oxide Anchored on an Ultrasonically Exfoliated Porous Graphitic Carbon Nitride Nanosheet. *RSC Adv.* **2024**, *14* (31), 22063–22075. https://doi.org/https://doi.org/10.1039/d4ra03096f

(57) Chougale, R. K.; Sanadi, P. D.; Patil, S. S.; Siddharth, U. S.; Pawar, P. P.; Bhosale, B. D.; Kamble, G. S. Water-Hyacinth-Leaf-like 2D Bismuth Oxychloride Photocatalyst for the Degradation of Methylene Blue and Crystal Violet Dyes. *RSC Adv.* **2026**, *16* (18), 16181–16193. https://doi.org/https://doi.org/10.1039/d6ra01208f

(58) Hayati, F.; Maslaki, S. A.; Shirazi, M. M. A.; Brinkmann, M.; McPhedran, K. N. Photocatalytic Degradation of the Tire-Derived Chemical 1,3-Diphenylguanidine in

Stormwater Using a Biochar-Supported NZn Doped TiO2 Catalyst. *Chem. Eng. J.* **2026**, *547*, 181051. https://doi.org/https://doi.org/10.1016/j.cej.2026.181051

(59) Bibi, S.; Bashir, A.; Tabassum, N.; Lee, I. E.; Yasmeen, H.; Abbas, S. M.; Wali, Q.; Aamir, M.; Ko, C.; Ahmad, I. Sunlight-Driven Fast Photo-Degradation of Eriochrome Black T Dye Using Highly Efficient La-Doped Ag3PO4 Decorated with ZnS QDs. *RSC Adv.* **2026**, *16* (25), 23136–23153. https://doi.org/https://doi.org/10.1039/d6ra00544f

(60) Li, L.; Li, J.; Kim, B.-H.; Huang, J. The Effect of Morphology and Crystal Structure on the Photocatalytic and Photoelectrochemical Performances of WO3††Electronic Supplementary Information (ESI) Available: See DOI: Https://Doi.Org/10.1039/D3ra07329g. *RSC Adv.* **2024**, *14* (3), 2080–2087. https://doi.org/https://doi.org/10.1039/d3ra07329g

(61) Ângelo, J.; Magalhães, P.; Andrade, L.; Mendes, A. Characterization of TiO2-Based Semiconductors for Photocatalysis by Electrochemical Impedance Spectroscopy. *Appl. Surf. Sci.* **2016**, *387*, 183–189. https://doi.org/https://doi.org/10.1016/j.apsusc.2016.06.101

(62) Cai, Q.; Hu, J. Decomposition of Sulfamethoxazole and Trimethoprim by Continuous UVA/LED/TiO2 Photocatalysis: Decomposition Pathways, Residual Antibacterial Activity and Toxicity. *J. Hazard. Mater.* **2017**, *323*, 527–536. https://doi.org/https://doi.org/10.1016/j.jhazmat.2016.06.006

(63) Liu, X.; Wang, J. Decolorization and Degradation of Crystal Violet Dye by Electron Beam Radiation: Performance, Degradation Pathways, and Synergetic Effect with Peroxymonosulfate. *Environ. Pollut.* **2024**, *350*, 124037. https://doi.org/https://doi.org/10.1016/j.envpol.2024.124037

(64) Cai, Q.; Hu, J. Decomposition of Sulfamethoxazole and Trimethoprim by Continuous UVA/LED/TiO2 Photocatalysis: Decomposition Pathways, Residual Antibacterial Activity and Toxicity. *J. Hazard. Mater.* **2017**, *323*, 527–536. https://doi.org/https://doi.org/10.1016/j.jhazmat.2016.06.006

(65) Xekoukoulotakis, N. P.; Drosou, C.; Brebou, C.; Chatzisymeon, E.; Hapeshi, E.; Fatta-Kassinos, D.; Mantzavinos, D. Kinetics of UV-A/TiO2 Photocatalytic Degradation and Mineralization of the Antibiotic Sulfamethoxazole in Aqueous Matrices. *Catal. Today* **2011**, *161* (1), 163–168. https://doi.org/https://doi.org/10.1016/j.cattod.2010.09.027

(66) Materials-17-01029 (1).

(67) Abellán, M. N.; Bayarri, B.; Giménez, J.; Costa, J. Photocatalytic Degradation of Sulfamethoxazole in Aqueous Suspension of TiO2. *Appl. Catal. B Environ.* **2007**, *74* (3), 233–241. https://doi.org/https://doi.org/10.1016/j.apcatb.2007.02.017

(68) Kundu, A.; Betzalel, Y.; Yaniv, V.; Vadivel, V. K.; Mamane, H. ZnO-Coated Nickel-Copper Foams for Dual-Function Photocatalytic Degradation of Pharmaceuticals and Pathogen Inactivation in Water. *J. Environ. Chem. Eng.* **2026**, *14* (1), 120595. https://doi.org/https://doi.org/10.1016/j.jece.2025.120595

(69) Sarasino, L.; Calavita, V. M.; Lagostina, V.; Calza, P.; Paganini, M. C. Enhanced Radical Formation and Water Purification via Lanthanide-Nitrogen Co-Doped Strontium Titanate. *Mater.* **2025**, *9*, 101041. https://doi.org/https://doi.org/10.1016/j.nxmate.2025.101041

(70) He, H.; Wang, W.; Xu, C.; Yang, S.; Sun, C.; Wang, X.; Yao, Y.; Mi, N.; Xiang, W.; Li, S.; Liu, G. Highly Efficient Degradation of Iohexol on a Heterostructured Graphene-Analogue Boron Nitride Coupled Bi2MoO6 Photocatalyst under Simulated Sunlight. *Sci. Total Environ.* **2020**, *730*, 139100. https://doi.org/https://doi.org/10.1016/j.scitotenv.2020.139100

(71) Salem, N. M.; Awwad, A. M. Biosorption of Ni(II) from Electroplating Wastewater by Modified (Eriobotrya Japonica) Loquat Bark. *J. Saudi Chem. Soc.* **2014**, *18* (5), 379–386. https://doi.org/10.1016/j.jscs.2011.07.008

(72) Han, R.; Zhang, J.; Han, P.; Wang, Y.; Zhao, Z.; Tang, M. Study of Equilibrium, Kinetic and Thermodynamic Parameters about Methylene Blue Adsorption onto Natural Zeolite. *Chem. Eng. J.* **2009**, *145* (3), 496–504. https://doi.org/https://doi.org/10.1016/j.cej.2008.05.003

(73) Gaffer, A.; Ebada, A.; Alawady, A. R. Rapid Microwave Assisted RAFT Synthesis of Amphiphilic HEMA-Co-AMPS Copolymers for High Performance Cu2+ and Cr6+ Removal from Water. *Sci. Rep.* **2026**, *16* (1), 10942. https://doi.org/10.1038/s41598-026-41634-9

(74) Rashad, S.; Farghali, A. A.; Halmy, M. W. A.; Elkady, H.; Badr, N.; Hassan, A.; Younes, H. A. High-Performance Activated Rice Straw Biochar: A Sustainable Triple-Bottom-Line Adsorbent for Removal of Water Pharmaceutical Pollution. *RSC Adv.* **2026**, *16* (26), 24157–24173. https://doi.org/10.1039/D6RA00965D

(75) Shi, Y.; Liu, G.; Wang, L.; Zhang, H. Activated Carbons Derived from Hydrothermal Impregnation of Sucrose with Phosphoric Acid: Remarkable Adsorbents for

Sulfamethoxazole Removal. *RSC Adv.* **2019**, *9* (31), 17841–17851. https://doi.org/10.1039/C9RA02610J